Ab Initio Prediction of Metal Phosphide Anode Materials for Lithium and Beyond Lithium Batteries

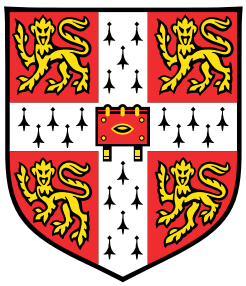

Angela Faye Harper

Supervisor: Dr. Andrew J. Morris

Department of Physics
University of Cambridge

This dissertation is submitted for the degree of
Master of Philosophy

Churchill College July 2018

Declaration

I hereby declare that this dissertation is the result of my own work and includes nothing which is the outcome of work done in collaboration except where specifically indicated in the text. This dissertation does not exceed the word limit of 15,000 words exclusive of tables, footnotes, bibliography, and appendices, as specified by the Degree Committee for the Faculty of Physics and Chemistry.

Angela Faye Harper
July 2018

Acknowledgements

I would like to thank my supervisor, Dr. Andrew Morris not only for his help and direction during this past year on my MPhil, but also for his encouragement in applying to Cambridge, and dedication to my career in physics. This year, I have done independent research properly for the first time, and felt confident in doing so, and I have his supervision to thank for that. Additionally, I would like to thank the members of the Morris group who have answered numerous questions throughout the year, without hesitation, especially Matt Evans, whose computational knowledge seems infinite. I would also like to thank Can and James, who I have shared an office with, for their conversations over coffee and at the whiteboard. And finally Bora, who I contacted around a year ago to discuss details of my project, and was my first introduction to the Morris group.

This research would not have been possible without funding and computing time, thus I would like to acknowledge my funding body, the Churchill Scholarship of America for giving me the opportunity to study at Cambridge, and for funding me to attend the American Physical Society March Meeting this year where I presented the work in this thesis. The calculations in this work were mainly carried out using time on the HPC Midlands+ machine, from a 1.2M core hour grant I was awarded from January to June of 2018. Smaller calculations were carried out on the BlueBear cluster at the University of Birmingham and on our own cluster.

Abstract

Identifying high capacity battery materials is critical for creating better energy storage to lower our reliance on non-renewable energy resources. While Li-ion batteries are the state-of-the-art, their graphite anodes are limited by a theoretical capacity of 372 mAh/g. Phosphorus is one alternative which has a high capacity of 2596 mAh/g and can alloy with both Li^+ and Na^+ ions, but suffers from large volume changes upon cycling. To mitigate this destructive effect, transition metals act as stabilising agents, limiting volume change and retaining high capacities. In this dissertation, I investigate two classes of transition metal phosphides (TMPs) as candidates for high capacity Li and Na-ion battery anodes. Herein, I employ a computational approach which combines density-functional theory (DFT) with structure searching methods including *Ab Initio* Random Structure Searching (AIRSS) and Genetic Algorithms (GA). I conduct an AIRSS and GA search of the Li-Cu-P system, as well as an AIRSS search of the Na-Fe-P system, and study their ground state electrochemical properties with DFT.

I investigate the lithiation pathway in Cu-P, and find that LiCu may form during cycling, increasing the overall capacity of all Cu-P anodes. Additionally, I calculate the capacity of CuP_{10}, to be 2225 mAh/g, while the highest capacity Cu-P to date is CuP_2 at 1495 mAh/g. This suggests that it should be tested in future experimental work. Using AIRSS, I identify a ground state Imm2 Cu_2P structure, which has not been identified experimentally, and find it is a stable semimetal at high temperature and pressures up to 10 GPa. I also find an AIRSS identified structure of Cu_3P with Cu vacancies (Cu_8P_3) which has different vacancy orderings to previously identified $Cu_{3-x}P$, suggesting this structure has several possible ground state orderings. Finally, I assess the effects of pressure on Cu-P, and find that several GA-identified $P1$ structures are low in energy at high pressure, suggesting they may form during extreme conditions on the battery anode.

To conduct an AIRSS search on the Fe-P system, I investigate the possible ways to introduce spin polarisation into the search, and determine that breaking the spin state on each atom can be included as a post-processing step of high-throughput searching. Furthermore, the experimental sodiation pathway for FeP_4 has not yet been identified, though it was considered to be a conversion anode. From the results of the ternary AIRSS search on Na-Fe-P, I propose a theoretical sodiation pathway via an insertion process for FeP_4 which includes an as-yet unidentified Pm ternary compound, NaFeP which may limit the overall battery capacity by 298 mAh/g.

Table of contents

Chapter 1

Introduction

1.1 The global importance of batteries

At the 2016 Paris climate accord, 194 nations and the European Union set a goal to limit the global temperature increase to 1.5 ^{o}C; this ambitious task is equivalent to removing 16 to 19 billion metric tons of CO_2 per year by 2030 [1, 2]. To make this a reality, countries will need to start both relying more on renewable sources of energy such as solar power, and supplementing gasoline-powered modes of transportation. However, the technology currently available in this area has several limitations, which prevent it from being a successful alternative to non-renewable energy sources. At best, solar energy can only be collected during the day, and thus a method for storing this energy is necessary for it to be utilised 24 hours a day, and during inclement weather. Transportation is an integral part of everyday life, which at the present time relies heavily on non-renewable fuel sources. Gasoline powered engines can travel several hundreds of miles without refuelling, and to be competitive, the electric alternative will need to provide a similar level of mileage or have a facile refuelling mechanism. While hydrogen storage is one possible answer, and indeed hydrogen fuel cell vehicles have entered the market, this method still requires hydrogen to be harvested to power the vehicles. Batteries on the other hand can use electricity from any source, such as solar or wind power, making them a more versatile renewable resource. Their limitation at the present time is the low amount of energy stored in a single battery cell. To create a future in which green energy is widely used, research into higher capacity batteries, which are able to store larger amounts of energy is desperately needed.

Batteries are used to store energy, such as that from a solar cell or power plant, and later convert that chemical energy into a usable electric form. A battery is comprised of electrochemical cells which are connected to increase the overall battery voltage and capacity. Batteries are classified as either primary or secondary, depending on whether the cells in the battery are non-rechargeable or rechargeable, respectively. For applications such as powering cars or houses, it is imperative to have a rechargeable battery, to allow cars to make multiple

trips, and permit grid scale storage. One example of a rechargeable battery, which will be the focus of the rest of this work, is the Li-ion battery. This technology, which uses a "rocking-chair" technique to transport ions, was pioneered in the 1980s by Goodenough, and sold in the 1990s by Sony, making it commonplace in most technologies over the last two decades [3]. In most cases today, the Li-ion battery is the battery of choice for many high energy and power applications [4].

A schematic of a Li-ion cell is shown in Figure 1.1, with the main parts of the cell labelled. The cathode (positive electrode) is the source of Li^+ ions in the cell, and is a layered-oxide structure such as $LiCoO_2$. The anode (negative electrode) is a material, such as graphite, which accepts these ions. Depending on the type of anode used, the ions can undergo an alloying, conversion, or intercalation process. When the battery is charged, Li^+ ions flow through the liquid or polymer electrolyte, to the anode while electrons flow from the cathode to the anode through the external circuit where a device (such as a portable electronic, or electric vehicle) is connected. In this rechargeable battery, the opposite reaction is also possible, allowing the anode material to be reduced and ions to flow back through the electrolyte to the cathode, while electrons power the outer device. This reaction is driven by the Li^+ chemical potential difference across the anode and cathode between the electrolyte. The cathode, being the host of Li, is a more favourable place for Li^+ ions to sit.

While these rechargeable Li-ion batteries have many benefits, there are several areas which require improvement. These include increasing the electrode capacity, creating solid-state electrolytes which attempt to prevent the formation of dendrites and are safer alternatives to the flammable and volatile liquid electrolytes, and moving beyond Li-ion to cost-effective and sustainable alternatives such as Na^+, or divalent ions such as Mg^{2+} [5, 6]. The focus of this work will be on conversion anode materials beyond graphite, for both Li-ion and Na-ion batteries. Graphite is a relatively inexpensive material with low volume expansion during lithiation but suffers from two main issues: firstly, graphite has a low theoretical capacity of 372 mAh/g, which is well below theoretical capacities of other anode materials. Given that this is the calculated upper limit, materials are needed with higher theoretical capacities to accommodate a need for longer-lasting battery materials in grid scale storage and transport applications [6, 7]. Secondly, while cathode materials for Na-ion batteries were easily transferred from their Li counterparts (e.g. $LiCoO_2$ to $NaCoO_2$), graphite does not host Na^+ ions [8].

One possible alternative anode material is phosphorus, which has a theoretical capacity of 2596 mAh/g and the ability to intercalate both Na^+ and Li^+ ions [10, 11]. However, phosphorus is an alloying material which exhibits destructive levels of volume expansion upon lithiation and sodiation, and thus has a low cycle life [7]. Adding a transition metal (TM) to the anode starting structure, allows ternary phases of Li-P-TM or Na-P-TM to form, which could stabilise the overall conversion reaction, improving cyclability, and lowering volume expansion. This dissertation thus focuses on these materials, in a search for high capacity transition metal phosphorus derived anodes. Figure 1.2 shows the relative capacities of phosphorus metal

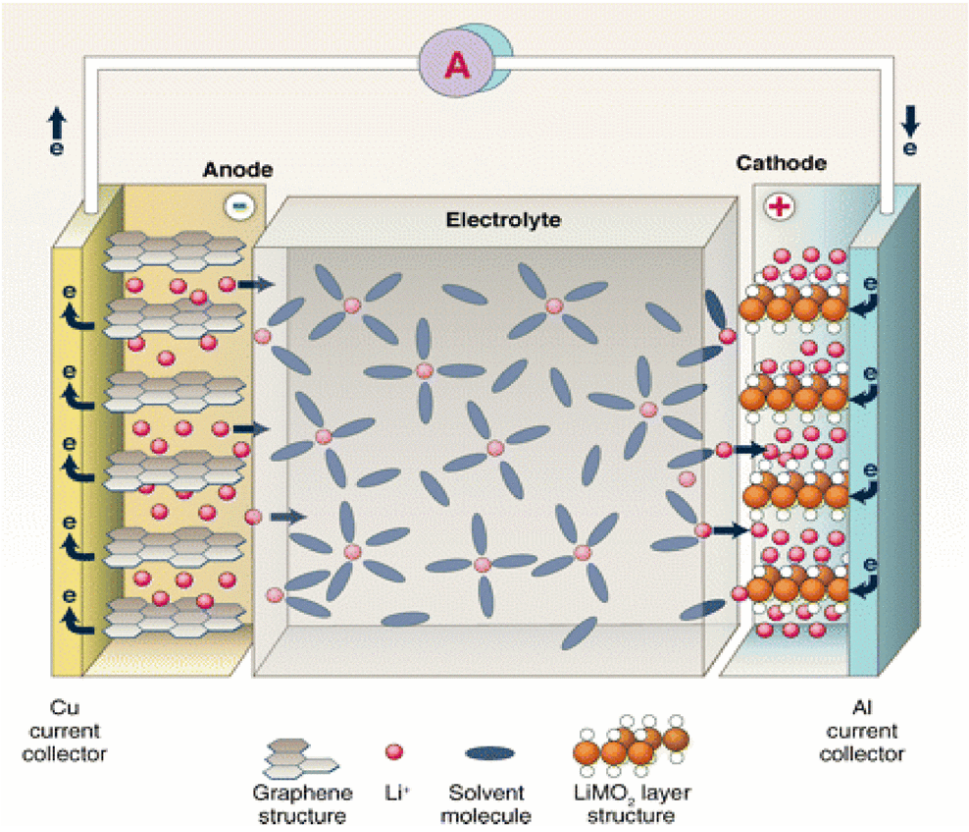

Fig. 1.1 Schematic of a Li-ion battery with a graphite anode (left), liquid electrolyte (centre), and $LiMO_2$, where M is a transition metal, cathode (right) with Li ions shown in red flowing from the anode to the cathode through the electrolyte, with electrons (blue "e") flowing around the outer circuit. This figure is adapted from [4] ©2011 IEEE.

compositions from the Open Quantum Materials Database (OQMD), which show the relative high capacities of phosphorus anodes compared to graphite. For these reasons, transition metal phosphides (TMPs) are a good choice to investigate, in order to find higher capacity, low-volume expansion alternatives to graphite anodes.

1.2 Transition metal phosphide anode materials

Most transition metal phosphide (TMP) materials are conversion anodes, which undergo a succession of chemical reactions when Li^+ ions enter the anode. The overall conversion reaction can be characterised by the equation

$$3x\ \mathrm{Li} + \mathrm{MP}_x \leftrightarrow \mathrm{M} + x\ \mathrm{Li_3P} \tag{1.1}$$

in which up to 3 Li^+ or Na^+ are inserted into the TMP. This conversion reaction is reversible and the overall capacity of the resulting reaction is directly related to the phosphorus content, as in these cases the metal is inactive and thus does not contribute to the battery capacity.

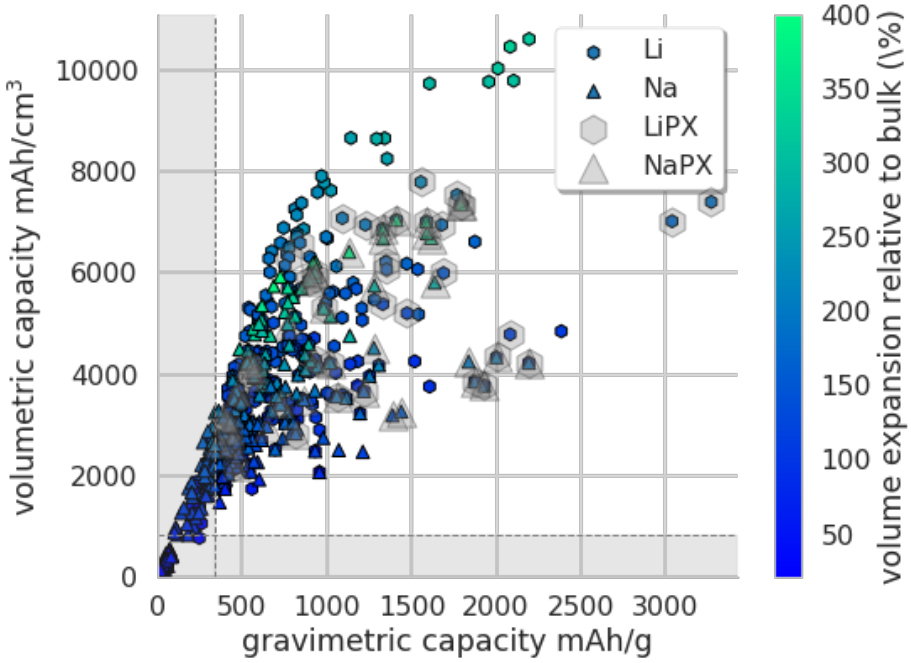

Fig. 1.2 Transition metal pnictide (Group 15) elements and their relative gravimetric and volumetric capacities with respect to both Li^+ and Na^+ from the OQMD [9]. Transition metal phosphides (TMPs) are in grey, and the other circles are coloured with respect to their volume expansion. All TMPs are higher in volumetric and gravimetric capacity than graphite, which is shown at the intersection of the two crossed lines on the bottom left.

The following chapters will thus focus on two of these transition metal phosphides, copper-phosphorus and iron-phosphorus.

The copper phosphides have been widely studied in Li-ion batteries, especially by the Monconduit group [12–14]. Of the four known copper phosphides, a $P2_1/c$ phase of CuP_2 and a $P6_3cm$ phase of Cu_3P exhibited successful Li^+ intercalation [15–17]. Cu_3P had an initial discharge capacity of 415 mAh/g, with a stable capacity of around 200 mAh/g [15]. It was noted that after the first cycle, XRD spectra suggested that an amorphous structure was reformed after cycling, as the initial hexagonal structure of Cu_3P was not detected. The performance of Cu_3P is lower than graphite, and thus is unlikely to replace graphite. However, Cu_3P has a consistent cyclability and thus is attractive for specialised uses which may require low cycle rates and moderate capacity. In contrast, CuP_2 delivers an initial capacity on the first discharge cycle of 1325 mAh/g, which fades to only 360 mAh/g after 10 cycles [17]. While both CuP_2 and Cu_3P had cyclability issues on their own, embedding CuP_2 in a carbon composite improved cyclability between 604 mAh/g and 817 mAh/g after 100 cycles [18]. Similarly a Cu_3P and reduced graphene oxide nanocomposite material exhibited a reversible capacity of 756 mAh/g after 80 cycles [19]. This suggests with additional nanostructuring, the capacity of many copper phosphides can be improved. Given its instability in air, Cu_2P_7 has not been

experimentally tested [15]. Additionally, CuP_{10} has not yet been tested as an anode material, and was only identified once by Lange *et al.* as a polyphosphide structure derived from fibrous violet phosphorus [20]. Despite its low gravimetric capacity, the Cu_3P phase especially has shown great promise as a Li-ion battery anode, given its cycling stability and high volumetric capacity (4732 mAh/cm^3 compared to graphite's volumetric capacity of 830 mAh/cm^3), and by studying this family we have calculated the properties of the copper phosphide structures in more detail, to better understand their real-world applications.

In addition to copper, iron phosphides are interesting candidates for anodes particularly because of the abundance of Fe in the Earth's crust, making it a relatively low cost material. Furthermore, *P*mnn FeP_2, and $P2_1/c$ FeP_4 have been experimentally tested as anode materials for Li^+ ion batteries, in which FeP_2 exhibits a conversion reaction, while FeP_4 undergoes a poorly understood insertion reaction which has yet to be fully characterised [13]. Similarly, the same phases of FeP_2 and FeP_4 have been tested in Na^+ ion batteries, and while FeP_2 showed little reaction towards Na^+, FeP_4 had an initial sodiation capacity of 1417 mAh/g, which after 30 cycles remained stable at 1100 mAh/g [21]. In this case, the FeP_4 structure is clearly stable as a Na^+ ion anode, and has a high retention of capacity up to 30 cycles. While this is the only study on iron-phosphides for Na^+ ion anodes, given the low cost of Na, Fe, and P, this anode would be especially attractive for use not only in inexpensive electronic applications, but also for large scale grid storage, which is currently prohibited by price.

1.3 High-throughput computational materials design

Studying many diverse systems of materials is a time-intensive experimental process. However, this process can be strategically guided by using computational structure searching techniques to identify potential candidate structures of a given system based on specific computational metrics. In the case of battery anodes this includes a high theoretical capacity and low voltage vs. Li/Li^+ or Na/Na^+.

Several databases of crystal structures exist, such as the Materials Project, AFLOW, and OQMD, which contain a conglomerate of both experimental phases from the Inorganic Crystal Structure Database (ICSD), and novel theoretical phases [9, 22–24]. While this data is a useful starting point, it is necessary to conduct computational searches with accurate calculations, and in an exhaustive manner, focusing on selected systems to identify interesting materials in those systems. In this work, I study the transition metal phosphide binary or ternary system in detail in order to better understand those compounds within the wider context of chemistry, and even potentially suggest applications for the materials I study which extend beyond just battery anodes.

To evaluate the energies of each structure, I use density-functional theory (DFT) as a first test of stability for these materials. This theory is described in detail in Chapter 2, and is based

on quantum mechanical interactions between electrons within a periodic crystal. DFT has been widely used to study different material systems, and is a reliable first step towards identifying the ground-state structures within each transition metal phosphide system.

Previous studies by Mayo *et al.* of Li-P and Na-P identified the stable structures in both of these systems, and suggested voltage profiles for lithiation and sodiation [25]. This study attempts go to beyond those initial binary searches to identify ternary structures of both Li-Cu-P and Na-Fe-P, as well as understand the electronic and structural properties of ground-state structures in both the Cu-P and Fe-P TMP systems, which have yet to be studied using an *ab initio* exhaustive searching approach.

The crystal structure searching method employed herein is *Ab Initio* Random Structure Searching (AIRSS) , which has been previously successfully employed in lithium silicides and germanides, high-pressure phases of silane, and lithium and sodium phosphorus anodes [25–28]. Using this method, I have studied two families of transition metal phosphides in detail, identifying stable and metastable structures in each, and characterising these two systems using DFT.

The outline of the dissertation is as follows. Chapter 2 will discuss the methods and theory used to study both systems of TMPs, especially focusing on DFT, as well as the high-throughput computational searching technique AIRSS, and the metrics used to quantify these results in the context of battery materials. Chapter 3 will then address the copper phosphide system in detail, providing information on the ground-state structures of copper phosphides, which were identified using a combination of GA and AIRSS searches, as well as the effects of temperature and pressure on this system in the context of Li-ion batteries. Chapter 4 includes a study of the ternary Na-Fe-P system, with the results of a ternary Na-Fe-P AIRSS search as it relates to Na-ion batteries. Finally, Chapter 5 provides a discussion of the results in this dissertation, and presents potential future outlooks for this work.

Chapter 2

Methods and theory

2.1 Density-functional theory

In order to understand the electronic ground-state properties of materials in this dissertation, density-functional theory (DFT) is used. Using DFT, it is possible to calculate many properties of a material including the equilibrium crystal structure, volume, and energy, as well as the band structure and density of states of the electrons in the crystal structure. At its core, DFT is a method by which one can solve (with approximations described herein) the many-body time independent Schrödinger equation,

$$\hat{H}\Psi_n(\{\mathbf{R}_i\},\{\mathbf{r}_j\}) = E_n\Psi_n(\{\mathbf{R}_i\},\{\mathbf{r}_j\}), \tag{2.1}$$

for the ground-state energy of the system, E_0. In Equation 2.1, $\{\mathbf{R}\}$ are the positions of the nuclei, $\{\mathbf{r}\}$ are positions of the electrons, E_n are the energy eigenvalues, $\Psi_n(\mathbf{R}_i,\mathbf{r}_j)$ are the corresponding wave functions, and $\hat{H}$ is the Hamiltonian. Directly solving 2.1 for the wave functions quickly becomes computationally intractable for anything beyond a few particles, and so the following approximations are made to simplify the problem. The first is the Born-Oppenheimer approximation [29]. This approximation utilises the fact that the nuclei are orders of magnitude more massive than the electrons. The nuclei are essentially immobile on the timescale of electronic motion, and thus can be considered separately from the electrons. We can then rewrite the Schrödinger equation, taking into account only the position of electrons,

$$\hat{H_e}(\{\mathbf{R}_i\})\Psi_n(\mathbf{r}_j) = E_n\Psi_n(\mathbf{r}_j). \tag{2.2}$$

The nuclear positions $\{\mathbf{R}_i\}$ then enter this equation as parameters in $\hat{H_e}$. The resulting electronic Hamiltonian for such a system, is then defined as:

$$\hat{H}_e = \hat{T}_e + \hat{V}_{ee} + \hat{V}_{Ne} \tag{2.3}$$

where $\hat{T}_e$ is the kinetic energy of the electrons, $\hat{V}_{ee}$ is the electron-electron potential energy, and $\hat{V}_{Ne}$ is the electron-nuclei interaction.

While the Hamiltonian has been substantially simplified, finding a solution is still difficult, even for small systems, given that the possible form of $\Psi_n(\mathbf{r}_j)$, is unknown. In 1928, Hartree proposed a model, which attempts to solve Equation 2.2 for the wave function, using a mean-field approximation in which one electron experiences the effect of the surrounding electrons as an average distribution, thus treating electrons as independent particles [30]. However, electrons are indistinguishable fermions, and thus must obey the principle of electron exchange, in which the wave function is antisymmetric under particle exchange. Fock then introduced a Slater determinant of single particle orbitals,

$$\Psi(\boldsymbol{r}) = \frac{1}{\sqrt{N!}} \begin{vmatrix} \psi_1(\boldsymbol{r}_1) & \psi_2(\boldsymbol{r}_1) & \dots & \psi_n(\boldsymbol{r}_1) \\ \psi_1(\boldsymbol{r}_2) & \psi_2(\boldsymbol{r}_2) & \dots & \psi_n(\boldsymbol{r}_2) \\ \vdots & \vdots & \ddots & \vdots \\ \psi_1(\boldsymbol{r}_n) & \psi_2(\boldsymbol{r}_n) & \dots & \psi_n(\boldsymbol{r}_n) \end{vmatrix} \tag{2.4}$$

to anti-symmetrise the wave function so that it respects Pauli exclusion (i.e. electron exchange). The combination of particle exchange and the Hartree electrostatic potential is known as Hartree-Fock theory, and is still widely used in computational chemistry as post-Hartree-Fock methods such as coupled cluster theory or Møller Plesset theory [31, 32]. Solving equation 2.2 using this Slater determinant as the trial wave function, leads to a set of coupled one particle orbitals ψ_i. Applying the variational principle (i.e. energy minimisation) to these separated single particle orbitals now adds a Fock exchange term, V_i^x to each one particle Hamiltonian, such that

$$\hat{h}_i = -\frac{1}{2}\nabla^2 + V_{ext}(\mathbf{r}) + V_i{}^H(\mathbf{r}) + V_i{}^x \tag{2.5}$$

in which V^H is the Hartree potential,

$$V^H(\boldsymbol{r}) = \sum_j \int \frac{|\psi_j(\boldsymbol{r}')|^2}{\|\boldsymbol{r} - \boldsymbol{r}'\|} d^3\boldsymbol{r}' \tag{2.6}$$

where ψ_j is the single-particle wave function and $V_i{}^x$ is the non-local exchange term obtained by using the Slater determinant in Equation 2.4 as a trial wave function for minimising Equation 2.3. Hartree-Fock theory requires that one represent the wave function with a single Slater

determinant (i.e. the determinant of all single particle orbitals). In general the many-body wave function cannot be written as a single Slater determinant, but is rather a sum of infinite Slater determinants. As a result, Hartree Fock theory does not account for electron correlation, since in most cases all wave functions will not be accounted for in a single determinant, and thus the resulting Hartree-Fock energy will over estimate the true ground-state energy.

The following two theorems by Hohenberg and Kohn, which formulate the basis of DFT, attempt to work around the problem of not accounting for electron correlation by introducing the concept of the electron density $n(\mathbf{r})$, and proving that the ground-state energy of the system could be determined from $n(\mathbf{r})$, without the use of the many-body wave function [33]. By using the electron density as the quantity of interest this reduces the problem down from a solution of order $3N$ (where N is the number of electrons) to a solution of three spatial variables. The first theorem states that the external potential $\hat{V}_{ext}$ and the total energy E in a system of interacting particles can be written as a universal functional of the electron density $n(\mathbf{r})$:

$$E[n(\mathbf{r})] = F[n(\mathbf{r})] + \int V_{ext}(\mathbf{r}) n(\mathbf{r}) d^3\mathbf{r}. \tag{2.7}$$

The functional is due to the kinetic and potential energy electron terms in equation 2.3, and is written as:

$$F[n] = \langle \Psi | \hat{T} + \hat{V}_{ee} | \Psi \rangle, \tag{2.8}$$

The second theorem states that for a given $V_{ext}(\mathbf{r})$, the exact ground-state energy of the system is a global minimum of the functional in Equation 2.8, and the density $n(\mathbf{r})$ which minimises the functional is the exact ground-state density $n_0(\mathbf{r})$. Thus determining $F[n(\mathbf{r})]$ determines the solution to Equation 2.2. Of course, in general $F[n(\mathbf{r})]$ is not known, and thus determining approximations to $F[n(\mathbf{r})]$ is the basis of much of DFT.

To attempt to solve this problem, Kohn and Sham went on to rewrite Equation 2.7 as [34]:

$$E[n(\mathbf{r})] = T_0[n(\mathbf{r})] + \int \left(V_{ext}(\mathbf{r}) + \frac{1}{2} V_H(\mathbf{r}) \right) n(\mathbf{r}) d^3\mathbf{r} + E_{xc}[n(\mathbf{r})] \tag{2.9}$$

where T_0 is the non-interacting kinetic energy, V_H is the Hartree potential from Equation 2.6, and E_{xc} is the exchange-correlation functional. E_{xc} represents the difference between the exact energy of the system and the calculated energies, and its precise form is unknown. Equation 2.9 is solved by writing $n(\mathbf{r})$ as a sum of one electron wave functions $\psi_i(\mathrm{r})$ such that $n(\mathbf{r}) = \sum_i |\psi_i(\mathbf{r})|^2$. The total energy is then found by minimising $E[n(\mathbf{r})]$ subject to the constraint that the ψ_i remain orthonormal. This gives us the Kohn-Sham equations:

$$\hat{H}_{KS}[n]\psi_i(\mathbf{r}) = e_i\psi_i(\mathbf{r}) \tag{2.10}$$

where H_{KS} is given by:

$$H_{KS} = -\frac{1}{2}\nabla^2 + \hat{V}_{ext}[n] + \hat{V}_H[n] + \hat{V}_{xc}[n] \tag{2.11}$$

These equations have a clear interrelation since the choice of $n(\boldsymbol{r})$ leads to a different $E_{xc}[n](\boldsymbol{r})$, which in turn leads to a different ground-state wave function $\psi_i(\boldsymbol{r})$, and since $\sum_i |\psi_i(\mathbf{r})|^2 = \mathrm{n}(\mathbf{r})$, this leads to a new $n(\boldsymbol{r})$. This requires the use of a self-consistent process, iteratively solving for the ground-state energy, until input and output densities are the same, or have converged to a constant value within a certain tolerance.

2.1.1 Exchange correlation functional

The mathematical formalism having been constructed, the only remaining challenge of DFT is to calculate the exchange-correlation term E_{xc}. There are many approximations of increasing accuracy (and increasing computational effort) which attempt to reach chemical accuracy [35]. The first order approximation, known as the Local Density Approximation (LDA), is most accurate when the density is slowly varying throughout a crystal, as it only takes into account the density at single points [34]. The obvious extension of this, known as the Generalised Gradient Approximation (GGA) takes into account both the density and the gradient of the density at each point, and thus is especially applicable in systems where the density gradients are non-negligible at each point. GGAs are the most widely used functionals today in DFT. The general form of a GGA exchange correlation functional is,

$$E_{xc}^{\mathrm{LDA}}[n](\mathbf{r}) = E_{xc}^{\mathrm{GGA}}(n(\mathbf{r}), \nabla n(\mathbf{r})) \tag{2.12}$$

Beyond GGA, taking the Laplacian of the density using a Taylor series expansion is no longer viable, because the density gradients do not converge. While further so-called Hybrid Functionals are possible, which are a combination of GGA or LDA functionals and a Hartree-Fock exchange term, for the applications described in this dissertation, the GGA functional known as Perdew-Burke-Ernzerhof (PBE) will be applied [36].

2.1.2 Plane-Waves and pseudopotentials

Plane-wave DFT, which will be applied here, calculates the ground-state wave functions of a system, by treating the system as a periodic crystal in which the boundary conditions assume an infinitely repeating crystal [37]. This theorem, known as Bloch's theorem, states that the eigenstates of a periodic operator, such as the electronic Hamiltonian $\hat{H}_{KS}$, can be chosen as eigenstates of the translation operators of the periodic crystal. The wave functions are thus separated into a periodic term ($c_{\boldsymbol{k}+G}$) and a exponential term. The wave function at each point in a system can be described using a sum of plane-waves of the form [38],

$$\psi(\mathbf{r}) = \sum_{G} c_{\mathbf{k}+\mathbf{G}} \exp(i\,(\mathbf{k}+\mathbf{G})\cdot\mathbf{r}) \tag{2.13}$$

By using plane waves, it is possible to converge the calculations for a given basis set by increasing the cutoff energy, $\mathrm{E_{cut}}=\frac{1}{2}|\boldsymbol{k}+\boldsymbol{G}|^2$ until the resulting ground-state energy is essentially unchanged.

To sample a sufficient number of **k**-points in an unbiased manner, it is common to use a grid such as a Monkhorst-Pack grid [39], in which a spacing between k-points is specified (in 2π Å^{-1}). From this spacing, a grid of **k**-points is chosen over the Brillouin zone, or the Wigner-Seitz cell of the reciprocal lattice, according to the formula

$$\mathbf{k}_{n_1,n_2,n_3} = \sum_{i}^{3} \frac{2n_i - N_i - 1}{2N_i}\mathbf{G}_i \tag{2.14}$$

Equation 2.14 defines a simple method for identifying **k**-points which contain all of the symmetry relations of the crystal lattice in reciprocal space, and allows for integration over the entire Brillouin Zone using a finite set of points. In cases of metallic systems, which include many transition-metal phosphides, it is important to sample a dense **k**-point grid in order to converge the overall energy of the system.

The convergence of a plane wave basis set is dependent on the number of plane waves used. However, given that these plane waves are non localised, the number of plane waves used could be quite large, to account for large oscillations in the final shape of the orbitals. Wave functions near the core will have large oscillations to enforce orthonormality to the core state wave functions, and thus a large number of plane waves is necessary to represent these wave functions oscillation. Pseudopotentials, are a way of reducing the number of plane waves used by treating the core electrons of atoms as frozen in the crystal, while allowing the valence electrons, which are most crucial for bonding, to relax during the calculation. By including less plane waves, and using a smoother potential function, we are able to improve computational efficiency and while retaining accuracy.

Many different kinds of pseudopotentials are available, with varying levels of efficiency and accuracy. One example are the accurate norm-conserving pseudopotentials in which the all-electron and pseudopotential wave functions agree beyond a chosen cutoff R_c (where R_c

is a chosen distance from the nucleus). The integrals for $r < R_c$ of both the all-electron and pseudopotential charge densities are equivalent, so as to provide a correct charge within the core region of the pseudopotential [40]. On the other end of the computational efficiency spectrum are the ultrasoft pseudopotentials (used in this work) in which the norm-conserving requirements are partially lifted, to allow for a "softer" core region in which the integral of the wave functions are not required to be equivalent, thus allowing the cutoff energy to be reduced [41]. The softness also means that fewer **G**-vectors are required to solve for the wave functions, which improves computational efficiency. Calculations which have converged **k**-points, **G**-vectors, and accurate pseudopotentials will provide the most precise results, and thus it is important to converge energies and forces with respect to the system in question.

2.2 Applications of DFT

All of the DFT calculations in this work were performed using CASTEP [42, 43]. While this code has many different functionalities including NMR spectroscopy and electron energy loss spectroscopy, the main applications to the systems in this dissertation are geometry optimisation (described in section 2.3.1), band structure and phonon calculations, and calculations which include spin polarisation and spin-orbit coupling.

2.2.1 Electronic band structure calculations

For each wave vector **k**, a set of energy levels can be obtained such that,

$$\hat{H}_{KS}\psi_{n,k} = E_{n,k}\psi_{n,k}. \tag{2.15}$$

From these $E_{n,k}$, a band structure can thus be generated which describes the accessible energy states at each **k**-point within the Brillouin Zone. A knowledge of these bands within the first Brillouin Zone is sufficient to describe the accessible energies throughout the periodic crystal.

Rather than sampling a large set of **k** vectors within the Brillouin Zone, it can be useful to restrict the calculation of energies to a set of special **k** points, which represent the highest symmetry components of the Brillouin Zone using the least number of points, to reduce the computational time needed for the calculation, and obtain a unique representation of the symmetry of the crystal [44]. A collection of these representations is implemented in the SeeK-path code by Hinuma, *et al.* and is used throughout this dissertation to provide the high symmetry points in the lattice [45].

Additionally, the Kohn-Sham wave functions generated at a given $E_{n,k}$ provide an orbital representation of the system. While the DFT orbitals are not equivalent to those described by a many-body wave function, their visualisation is useful for understanding chemical bonding within a material.

Several experimental techniques, including X-ray absorption spectroscopy, photoemission spectroscopy, and angle-resolved photoemission spectroscopy can give accurate electron densities in synthesised crystals, and can provide a useful comparison to the band structure calculations obtained from DFT.

2.2.2 Phonons and lattice dynamics

A description of the lattice dynamics from the static lattice gives an approximation of the entropy and energetic contributions to the overall free energy of the system, which provides an approximation of phonon effects at finite temperature. Expanding the total energy of the system about the Cartesian coordinates of the nuclei $\{\mathbf{R}_i\} = \alpha$ in a Taylor expansion, and limiting the number of terms to second order (the Harmonic Approximation) gives a representation of the total energy [46],

$$E = E_0 + \sum_{i,\alpha} \frac{\partial E}{\partial \boldsymbol{u}_{i,\alpha}} \boldsymbol{u}_{i,\alpha} + \frac{1}{2} \sum_{i,\alpha,j,\beta} \boldsymbol{u}_{i,\alpha} \frac{\partial^2 E}{\partial \boldsymbol{u}_{i,\alpha} \partial \boldsymbol{u}_{j,\beta}} \boldsymbol{u}_{j,\beta} \tag{2.16}$$

where $\boldsymbol{u}_{i,\alpha}$ are the atomic displacements away from equilibrium about each Cartesian direction. The second derivative appearing in Equation 2.16 is known as the force-constant matrix, and is denoted by $\Phi_{i,j}^{\alpha,\beta}$. The first order term goes to zero at equilibrium, since the forces are zero. This equation is solved by assuming periodic boundary conditions, and solutions of the form,

$$\boldsymbol{u}_{i,\alpha} = \epsilon_{i,\alpha} \exp[i(\boldsymbol{q} \cdot \boldsymbol{R_i} - \omega t)] \tag{2.17}$$

where $\boldsymbol{q}$ is the phonon wave vector and ϵ is the polarisation vector. The above two equations then lead to the eigenvalue problem

$$\sum_{i,\alpha} D_{\alpha,\beta}^{i,j} \epsilon_{i,\alpha} = \omega^2 \epsilon_{j,\beta} \tag{2.18}$$

where the dynamical matrix, D, is

$$D_{i,j}^{\alpha,\beta}(\boldsymbol{q}) = \frac{1}{\sqrt{m_i m_j}} \sum_{\alpha} \Phi_{i,j}^{\alpha\beta} e^{-i\boldsymbol{q}\cdot\boldsymbol{r}_\alpha} \tag{2.19}$$

The dynamical matrix, D, is the Fourier transform of Φ normalised by the particle masses. Solving this eigenvalue equation for metallic systems, such as transition metals, can be done through a finite displacement supercell method. This method, as implemented in CASTEP, perturbs each atom in the primitive cell in the positive and negative direction, and calculates Φ for that atom using the central difference of the forces in each direction. It then assumes a decaying effect on atoms throughout the supercell, given that the forces on atom i will be most affected by the nearest neighbour atoms, and this effect will lessen for atoms further away throughout the periodic crystal.

Once the phonon frequencies are obtained, the temperature-dependent Gibbs free energy is then calculated by,

$$G = E_{\text{total}} + k_B T \sum_{\boldsymbol{q},i} \ln\left[2\sinh\left(\frac{\hbar\omega_{\boldsymbol{q},i}}{2k_B T}\right)\right], \tag{2.20}$$

where the second term is the phonon free energy calculated from the frequencies over the Brillouin zone. These calculations give insight not only into the phonons in the crystal, but also the structural stability of the atomic configuration at finite temperature.

2.3 Crystal structure prediction

2.3.1 AIRSS

In order to calculate the above properties on the experimentally relevant structures, it is necessary to understand which structures are most likely to actually be observed. While many crystal structures found using chemical synthesis have been deposited into the Inorganic Crystal Structure Database (ICSD), the entire configuration space of structures calculated using DFT helps to identify meta-stable phases as well as ground-state structures for experimental comparison [24]. To sample this configuration space, the *Ab Initio* Random Structure Searching (AIRSS) method is employed [28].

The AIRSS method is outlined in Figure 2.1[1]. Starting from a structure of randomly arranged atoms in a box with periodic boundary conditions, atomic positions are relaxed using DFT to find the lowest energy structural configuration for that set of atoms. This process is repeated over thousands of structures and the lowest energy ones are taken as the possible stable and metastable geometries which are experimentally relevant.

A geometry optimisation step involves minimising the force acting on each atom in the cell, and in this case, this is done using the limited-memory Broyden Fletcher Goldfarb Shanno (LBFGS) algorithm, as implemented by CASTEP [48, 49]. This is an iterative method, in which an approximated Hessian matrix (H) of energy derivatives is updated at each step and is used to step the atomic positions x_i toward an energy minima. The true Hessian is:

$$H_{ij} = \frac{\partial^2 E}{\partial x_i \partial x_j} \tag{2.21}$$

While AIRSS may seem unlikely to provide reasonable ground-state structures, given that the number of local energy minima increases exponentially with the number of atoms, it is possible to reduce this configuration space by adding several chemically sensible constraints to the system [50, 28]. In the context of this work, those constraints include limiting the elements

[1] All structural representations of compounds throughout this dissertation are constructed using the VESTA software platform as cited here [47]

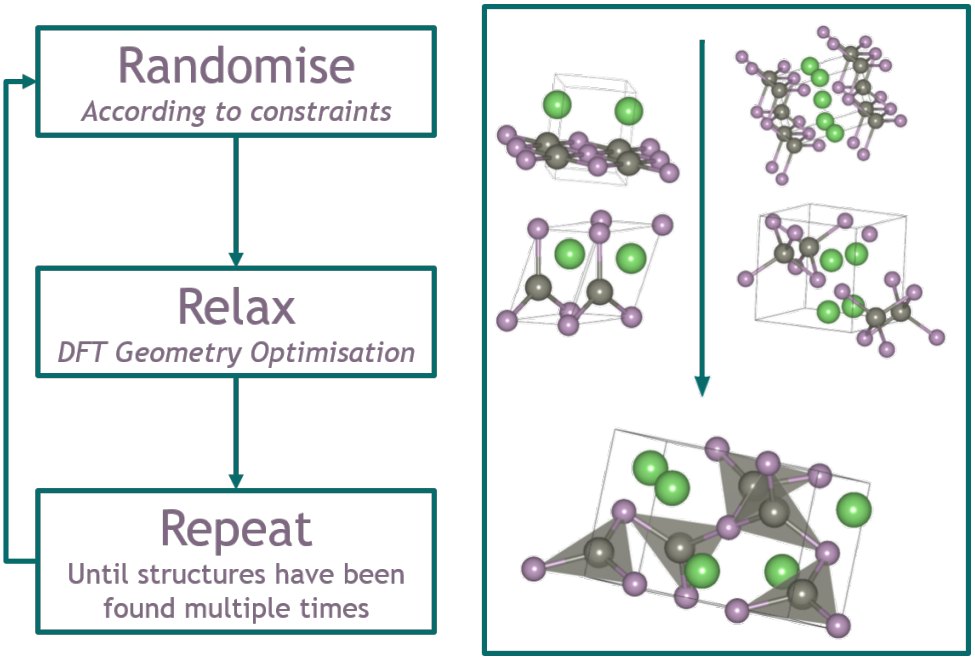

Fig. 2.1 Graphical representation of the AIRSS method for identifying ground-state crystal structures within a given system. Randomisation is subject to constraints such as minimum distance between atoms, types of atoms, etc. Relaxation is performed using DFT geometry optimisation.

to compounds in the groups of either Li-Cu-P systems or Na-Fe-P systems, placing a minimum separation between atoms to avoid overlap, constraining the maximum number of atoms in a box (usually around 40 atoms) and limiting the stoichiometries to, for example, compounds with between 1 and 5 atoms of each element. This is especially important in conducting a ternary search, as the search space is much larger in this context.

There are a wide variety of examples for which AIRSS has provided useful information about the chemistry of different systems. These include the high-pressure silane and aluminium phases [27, 51], defects in silicon [52, 53], and (relevant to this work) the phases of Na-P and Li-P formed during battery cycling as well as those formed in Sn anodes [25, 54].

2.3.2 Genetic algorithms

In addition to AIRSS, many other algorithms for crystal structure prediction exist including particle swarm optimisation and genetic algorithms [55, 56], and as more crystal structure databases such as the Materials Project have arisen, machine learning algorithms [57]. Each of these approaches requires a starting set of data, and given that AIRSS is able to efficiently and accurately provide a large set of low-energy structures, it is desirable to combine the AIRSS approach with another directed algorithm.

In this dissertation, AIRSS is combined with a simple “cut-and-splice” genetic algorithm, which takes a starting set of structures as the initial family and creates subsequent generations

by combining motifs in structures, adding interstitials, or introducing vacancies. At each step, structures are then geometry optimised using DFT, and the lowest energy structures are taken forward to the next generation to provide the new starting family. By introducing a GA, we are able to interpolate from the local structure identified with AIRSS, to find a potentially lower energy ground-state structure. This approach differs from AIRSS in that each step is dependent upon the previous step, and thus by using this method it is possible to access a more directed set of structures given a starting family. Especially in cases where many low-energy structures are low-symmetry or are layered, a genetic algorithm can identify structures which are lower in energy with these properties.

2.3.3 Thermodynamic phase stability

While a structure may be lowest in energy for a given stoichiometry, this does not necessarily imply that the structure is thermodynamically stable in relation to all other structures within that phase diagram. To find the ground-state at all stoichiometries, we can plot a convex hull of the formation energy of each stoichiometry, in relation to the elemental chemical potentials. For a binary structure A_xB_y the formation energy of the structure is calculated using:

$$E_f(A_xB_y) = E(A_xB_y) - xE(A) - yE(B), \tag{2.22}$$

where the energy of each structure is the DFT ground-state energy, and A and B are the chemical potentials of the system. Equation 2.22 is easily extended to ternary structures, $A_xB_yC_z$. To determine which phases are thermodynamically stable, the convex hull is constructed by plotting the composition versus formation energy per atom for each structure, as illustrated in Figure 2.2.

Figure 2.2 details an example of how the bottom tie-line of the hull is constructed. Before identifying the A_3B structure, A_2B had a formation energy which allowed it to sit on the convex hull between A and B (dotted line in Figure 2.2). By finding the A_3B structure at lower energy, the new hull (dark lines in Figure 2.2) no longer contains A_2B. In many cases this is where AIRSS and Genetic Algorithms can be useful, by identifying stable stoichiometries intermediate between the two chemical potentials.

2.4 Applications to batteries

AIRSS can be applied to many relevant systems, but in the case of this dissertation, battery materials, specifically conversion anodes are discussed, and so it is useful in this specific application to calculate several properties which are relevant to these materials, such as voltage profiles and gravimetric capacities.

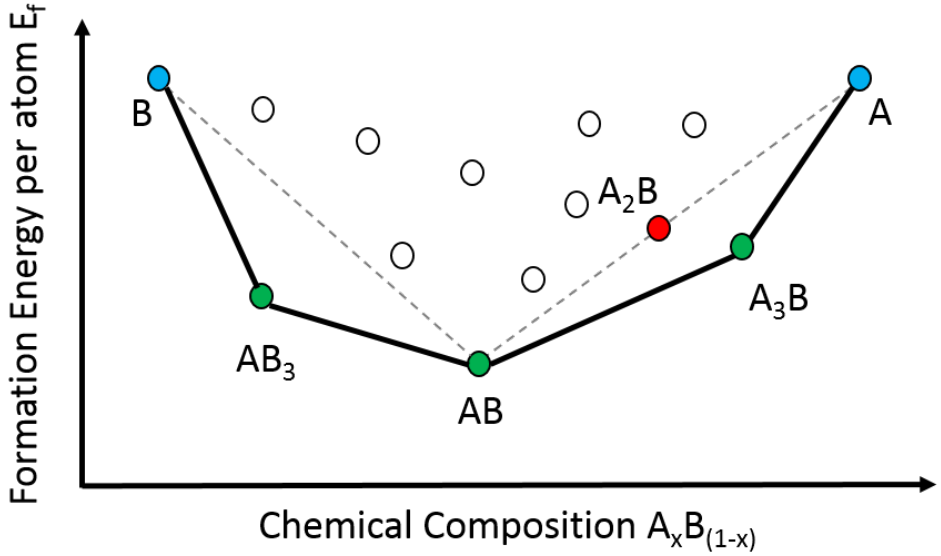

Fig. 2.2 Cartoon representation of a convex hull diagram for a fictitious binary structure A_xB_y. Points in green are those found on the convex hull tie-line, and are thermodynamically stable. The point in red is an example of a structure moved off the tie-line by another structure lower in formation energy, and points in white are those structures found above the tie-line, and are considered to be metastable.

2.4.1 Voltage profile

A binary or ternary convex hull provides the potential energy landscape of a system from which it is possible to calculate the relative voltages of a specific material in reference to a host ion (which in this case is either Li^+ or Na^+). The voltage is calculated according to [58],

$$V = -\frac{\Delta G}{x_2 - x_1} \approx -\frac{\Delta E}{x_2 - x_1} \tag{2.23}$$

where G is the Gibbs free energy of the system, and x_1 is the lithium content in the starting products, before lithiation occurs, and x_2 is the lithium content in the final products after lithiation. This is an approximation for the chemical equation,

$$\mathrm{Li}_{x_1}\mathrm{X} + (x_2 - x_1)\mathrm{Li} \longrightarrow \mathrm{Li}_{x_2}\mathrm{X} \tag{2.24}$$

At 0 K, the Gibbs free energy is approximated by the internal energy (E) since the thermal contributions are assumed to be small for temperatures close to 0K. However, using phonon calculations to approximate the Gibbs free energy would be a more appropriate quantity of interest when comparing voltage profiles to experiments at finite temperature, given that Gibbs free energy takes into account some temperature effects from the harmonic motion of atoms in the crystal.

For the conversion anodes discussed in this work, which undergo the specific overall chemical reaction during lithiation,

$$\mathrm{CuP}_x + 3x\mathrm{Li} \longrightarrow x\mathrm{Li_3P} + \mathrm{Cu} \tag{2.25}$$

this is more clearly laid out as

$$V \approx -\frac{\Delta E}{3x} \tag{2.26}$$

The above calculations for the voltage and capacity are shown for the entire reaction, but to get reactions for each step in the conversion process, the same methods can be used. In this ternary system, at each step in the chemical reaction, the voltage difference is calculated as in Equation 2.24, for the amount of Li added from the reactants to the products.

Finally the gravimetric capacity is calculated after determining the number of Li added from reactants to products by

$$C_{\text{gravimetric}} = \frac{FN_{\text{Li}}}{m_{\text{de-lithiated}}} \tag{2.27}$$

where F is the Faraday constant, $m_{\text{de-lithiated}}$ is the mass of the de-lithiated anode material and N_{Li} is the number of Li atoms per formula unit of reactants. By applying the equations above to the DFT ground-state convex hulls, it is possible to construct a chemical picture of how these anodes will operate in a cell, even for those that have yet to be tested, thus these results can be directly compared to experiments.

Studying battery materials, especially anodes, using both AIRSS and DFT is a well-established method and has provided several results which have been tested against experimental data. Most recently, the specific sodiation pathways for Na-P batteries were explored in a combined computational and experimental study, which showed the formation of P-helices during cycling [59]. In the Na-Sn system, the intermediate structures formed upon sodiation were also identified by stable and meta stable AIRSS identified structures, and confirmed with experiment using NMR [54]. Beyond these studies, lithium silicides and germanides, lithium phosphides, and ternary phases of Li-FeS_2 have all been identified by such computational methods, and confirmed with experiment [26, 25, 60]. Such successes have thus prompted me to study two more systems in detail computationally, which have experimental counterparts for adequate comparison of these results to the experimental data. In the following chapters, I will therefore use a combination of the methods described in this chapter to study the iron phosphide and copper phosphide systems in detail as they relate to battery anode materials.

Chapter 3

Copper phosphide anodes

The binary family of copper-phosphorus transition metal phosphides contains three compounds which have been identified several times experimentally, CuP_2 [61], Cu_3P [62] and Cu_2P_7 [63, 64]. In addition to these three structures, select computational studies, have identified Cu_2P [23, 65]. In one case, CuP_{10} was identified experimentally, though no known computational efforts have identified this structure [20]. Of these four known experimental structures, CuP_2 and Cu_3P are the only two which have been extensively tested in battery applications [66, 18, 67]. Herein I conduct a computational search for further copper-phosphorus materials as a way to assess the other known copper phosphides CuP_{10}, Cu_2P_7, and Cu_2P, for their potential application in Li-ion batteries, as well as in the broader context of the copper-phosphorus binary system. Additionally, I attempt to identify the lowest energy $Cu_{3-x}P$ structure, which matches with experimental results, as this is the most widely studied copper-phosphorus anode so far, and thus by probing its exact ground-state configuration, I attempt to understand why $Cu_{3-x}P$ is the most commonly used battery anode in this family [68]. Finally, these searches provide a large set of structures which can be used for computationally more expensive, but experimentally cheaper anodes in the iron phosphorus family studied in Chapter 4.

3.1 Cu-P binary search

The initial AIRSS search on around 4,000 copper phosphorus (from here referred to as Cu-P) structures, was carried out with a basis set containing plane-waves up to 300 eV, a 0.05 2π $Å^{-1}$ Monkhorst-Pack k-point grid, and using a set of efficient Vanderbilt ultrasoft pseudopotentials in CASTEP [28, 39, 41, 42]. In addition to AIRSS searches, structures of other transition-metal pnictides in the Open Quantum Materials Database (OQMD) were considered by substituting the elements in those structures for copper and phosphorus [9]. This was done using the `matador` software package[1]. All Cu-P structures from the OQMD were re-optimised with the

[1]The source code for this package and database implementation as well as other plotting and data analysis features can be found at `https://bitbucket.org/ml-evs/matador/src/master/`

same plane wave cutoff in the basis set, k-point spacing, and pseudopotentials in order to create the initial convex hull. Because CuP_{10} was not in the OQMD, it was not used in convergence testing, but the conventional cell of the same structure from the Materials Project Database was included in my final data-set [22].

Figure 3.1 shows the convergence tests using the Perdew-Burke-Ernzerhof (PBE) functional for both the Materials Studio library of ultrasoft pseudopotentials and the "on-the-fly" generated C9 ultrasoft pseudopotentials from CASTEP [36, 41, 42]. The C9 set of CASTEP ultrasoft pseudopotentials were generated on-the-fly using CASTEP v17.1, and have been shown to be more accurate than the Vanderbilt efficient ultrasoft potentials, but have lower computational efficiency [69]. Thus, the C9 set of pseudopotentials was only used to refine the AIRSS results after the initial search. From these tests, a plane wave cutoff of 300 eV and a Monkhorst-Pack k-point spacing of 0.05 2π Å^{-1} were chosen for the AIRSS searches, and subsequent calculations were performed using the C9 pseudopotentials with a plane-wave basis set cutoff of 500 eV and 0.03 2π Å^{-1} Monkhorst Pack k-point spacing, keeping the energy differences below 5 meV/atom relative to the chemical potential energies of Cu and P.

The initial AIRSS searches did not fully access the global minimum of Cu-P structures, as seen in Figure 3.2, in which the cyan points, which represent AIRSS structures, do not reach the convex hull tie-line of known structures from the ICSD. The most probable reason for this was that the cells for these structures were too large, and in the case of Cu_2P_7 and CuP_{10} the ground-state was a layered structure, which is difficult for AIRSS to identify. However, there were some structures from AIRSS searches which had negative formation energies relative to the Cu and P chemical potentials, and thus likely identified the local structural environment around the ground-state structures. To attempt to access the global minima, a Genetic Algorithm (GA) implemented through `matador`[2] was used with a starting family of AIRSS structures within 0.2 eV/atom of the convex hull. AIRSS is able to identify the local structure for a given stoichiometry, and thus by adding vacancies or interstitials, and combining results from AIRSS searches in a “cut-and-splice” manner, the GA is able to combine this local order into a lower energy ground-state structure. Two GA searches were performed, one for stoichiometries between Cu and CuP and the other between CuP and P, to separate the starting families into Cu-rich and P-rich, respectively. The selection rules for each generation were a mutation rate of 0.4, crossover rate of 0.6, with 10 generations of structures and a maximum population of 30 structures per generation with 20 surviving structures. The results of the GA search are shown in Figure 3.2 as green points. The GA was able to find a $P\bar{1}$ Cu_2P_7 structure, as well as several $Cu_{3-x}P$ structures (see Table 3.1). AIRSS identified an Imm2 Cu_2P structure, and the GA identified two more Cu_2P structures 0.2 meV above the convex hull with space group I4/mmm. Neither CuP_{10} nor CuP_2 were identified by any of the computational searching methods, but were on the hull from the ICSD.

[2]Genetic Algorithm by Matthew Evans with source found at `https://bitbucket.org/ml-evs/illustrado/`

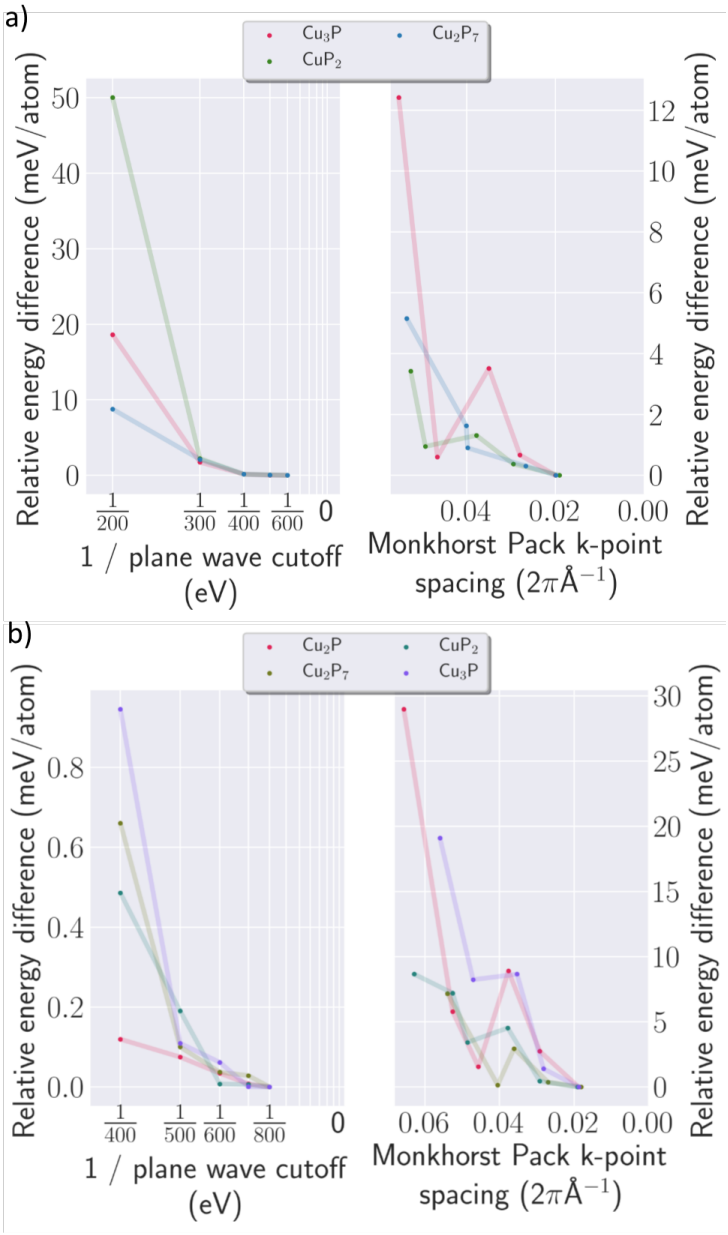

Fig. 3.1 The convergence test is done by comparing total energies at each plane wave cutoff and k-point spacing relative to the highest energy and smallest spacing. a) Convergence test of efficient Vanderbilt ultrasoft pseudopotentials for Cu-P structures from the OQMD. b) Convergence test of C9 CASTEP pseudopotentials for Cu-P structures from the OQMD.

All of the above calculations are done at the static lattice level, which does not take into account phonon effects which will be present at room temperature. Taking into account temperature effects could allow phases up to 50 meV off the hull at the static lattice level to be stabilised by phonons. Thus throughout, I will discuss phases at different cutoffs between 30 to 50 meV for each system. I have attempted to take a representative sampling of each family by choosing a cutoff within this range to analyse the structures.

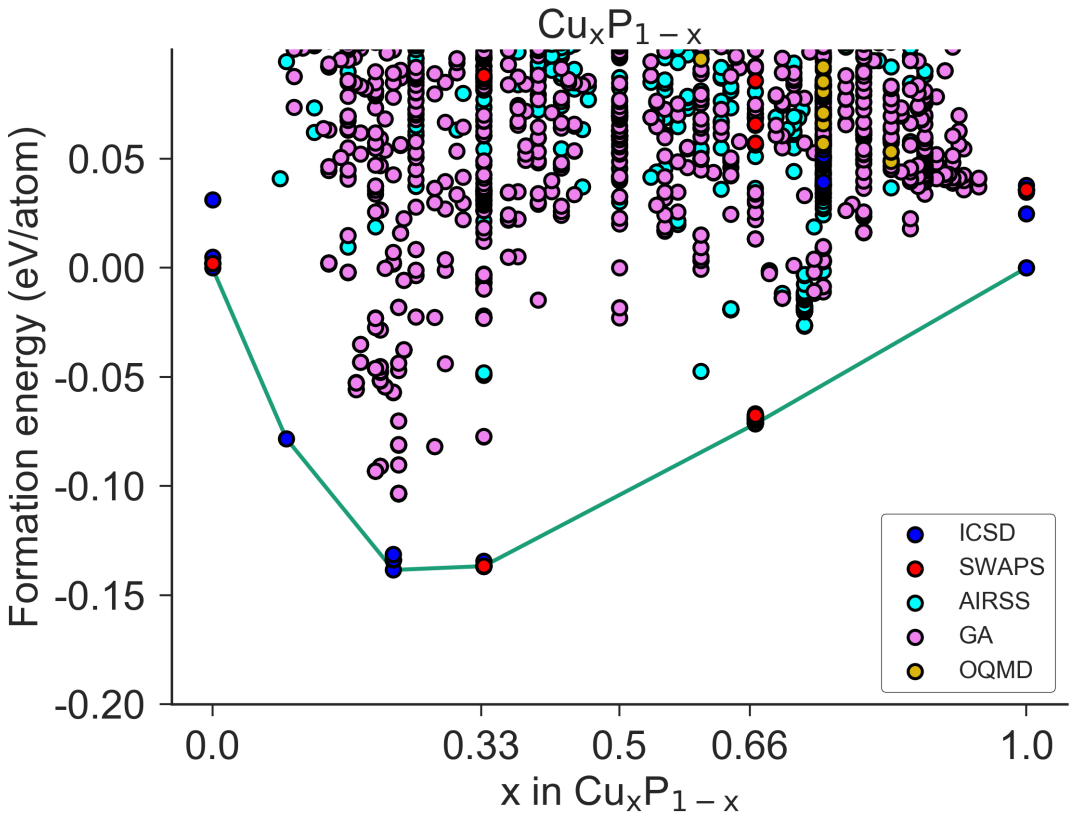

Fig. 3.2 Convex hull of structures between Cu and P. Geometry optimised at 300 eV cutoff, 0.05 Monkhorst Pack k-point spacing, with Vanderbilt ultrasoft pseudopotentials with points labelled by method used to identify structure. This figure shows the initial AIRSS and GA search to identify Cu-P structures, which will be discussed throughout the rest of the chapter in further detail.

Within 45 meV of the convex hull shown in Fig 3.2, there are 4 stable structures which lie on the tie-line shown in green, and 5 metastable stoichiometries. The structures with the lowest energy for each stoichiometry are shown in Table 3.1 and their crystal structures are shown in Figure 3.3. Most of these low energy structures are triclinic, with only one or two symmetry operations, except for Cu_2P, CuP_2, and Cu_8P_3. Both Cu_8P_3 and CuP_2 are monoclinic, and Cu_2P is orthorhombic.

A visual analysis of the crystal structures in Figure 3.3 highlights several structural relationship between the copper phosphides. $Cu_{17}P_6$ and Cu_8P_3 are both related, given their hexagonal symmetry. The ICSD form of Cu_3P, while higher in energy than the one pictured here has the same general structure (*P*63cm space group) as both Cu_8P_3 and $Cu_{17}P_6$, and later we will explore which vacancies in Cu_3P contribute to each of those structures. Finally, Cu_3P as shown here, is structurally similar to Cu_2P, as both have non-symmetric hexagonal lattices, shown in Figure 3.3. While Cu_2P has connected chains, Cu_3P has an added layer of Cu between the hexagonal rows of Cu and P.

In the bottom row of Figure 3.3, are several phosphorus rich compounds, all similar in structure and all from the same GA family tree. Though classified as $P1$ and $P\bar{1}$, they resemble the $C2/m$ ICSD structure of Cu_2P_7, suggesting a higher level of geometry optimisation would confirm their structural similarity. In the second row, both CuP_{10} and CuP_2 were not identified by either AIRSS or the GA. The high phosphorus content in CuP_{10} meant that initially it was outside the stoichiometric searching parameters of the AIRSS search, given that the initial search looked only for compounds of $Cu_{1-8}P_{1-8}$, and the layered structure suggests it would be difficult to find. CuP_2 presented difficulty on the other hand possibly because of the larger number of formula units (4 compared to 1 or 2 in most other structures). AIRSS was likely unable to find these structures because the initial searching parameters favoured highly ordered structures, such as Cu_2P. It is possible that a more extensive AIRSS search may find CuP_2 and CuP_{10}, but given that we already have their crystal structures from the ICSD, subsequent searches were not performed.

Material	Space Group	No. f.u.	Vol/f.u. (Å^3)	Hull dist. (meV/atom)	Provenance
Cu_3P	$P1$	2	50.8	42.8	GA
$Cu_{17}P_6$	Cm	2	283.8	45.2	GA
Cu_8P_3	$P2_1$	2	138.7	32.0	AIRSS
Cu_2P	$Imm2$	2	39.5	0.0	AIRSS
CuP_2	$P2_1/c$	4	46.8	0.0	ICSD
Cu_8P_{27}	$P1$	1	626.1	30.7	GA
Cu_2P_7	$P\bar{1}$	4	156.7	0.0	GA
Cu_7P_{27}	$P1$	1	623.1	36.1	GA
CuP_4	$P1$	7	88.7	31.4	GA
CuP_{10}	$P\bar{1}$	4	227.2	0.0	ICSD

Table 3.1 Lowest energy structures within 45 meV of the convex hull. Here f.u. is the number of formula units found within the ground-state structure.

In order to determine how these four Cu-P structures will change during cycling in a battery, it is also necessary to study the Cu-Li, Li-P, and ternary Cu-Li-P systems to identify all of the ground-state structures in those systems. From here we will proceed to construct the ternary phase diagram for this system, to study it fully in the context of the Cu-P phases being used as conversion anodes in a Li-ion battery.

3.2 Cu-Li binary search

In the experimental voltage profiles constructed for CuP_2 and Cu_3P, it has generally been assumed that no Cu-Li phases are present, and thus do not contribute to the overall capacity of the battery [12, 17, 66, 67]. While the exact geometry and stoichiometry of Li-Cu phases

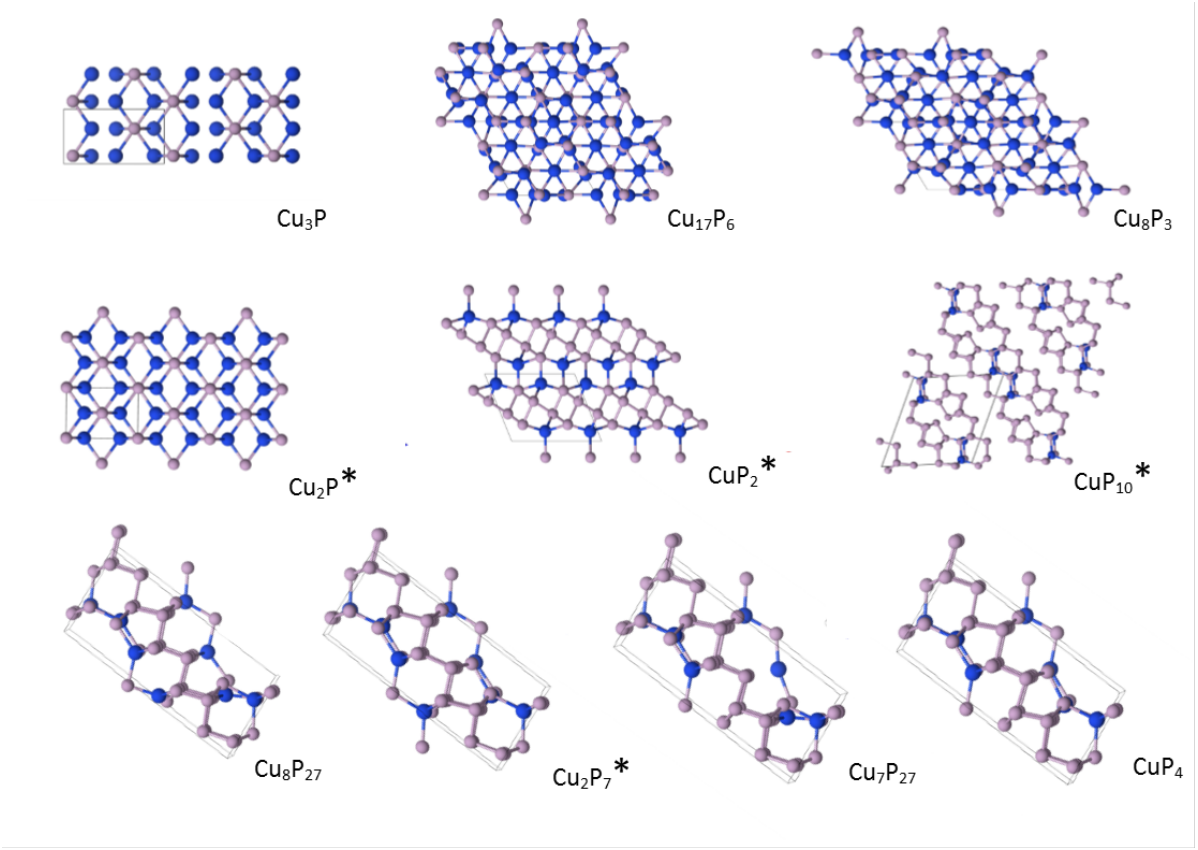

Fig. 3.3 Structures from Table 3.1 with Cu shown in blue and phosphorus in pink. Visually similar structures are grouped together. For example, $Cu_{17}P_6$ and Cu_8P_3, Cu_3P and Cu_2P. CuP_{10} shows similar characteristics to the four bottom structures, but in layered sheets. Structures labelled with an asterisk are those on the convex hull tie-line at the static lattice 0 GPa level.

are disputed in the literature, the existence of a Cu_4Li phase as well as a Cu_2Li_3 phase have been reported both experimentally and computationally [70–72]. Interestingly, the Materials Project and OQMD predict a $LiCu_3$ phase, and AFLOW predicts a Cu_2Li and Cu_7Li_6 phase, suggesting there are discrepancies even within the computational literature for this phase diagram [9, 22, 23]. By performing an AIRSS search, several other binary phases were identified at very low formation energies, and are discussed below. The existence of these phases could suggest additional possible pathways for copper-phosphides during lithiation.

Table 3.2 shows the lowest energy structures of each stoichiometry for those Li-Cu phases within 30 meV of the convex hull which are also lower in energy than the Cu or Li chemical potentials. Given that the hull itself is only 50 meV deep, this suggests that these structures are close in stability to both elemental Cu and Li, and thus may not form unless proper temperature and pressure conditions are found for each structure. It is also potentially unlikely that the Cu-Li compounds form during cycling, given that Cu is used as a current collector in most Li-ion graphite anodes, and so one would expect such compounds to form in conventional batteries. This could cause reduced capacity and poor performance if Li preferentially alloyed

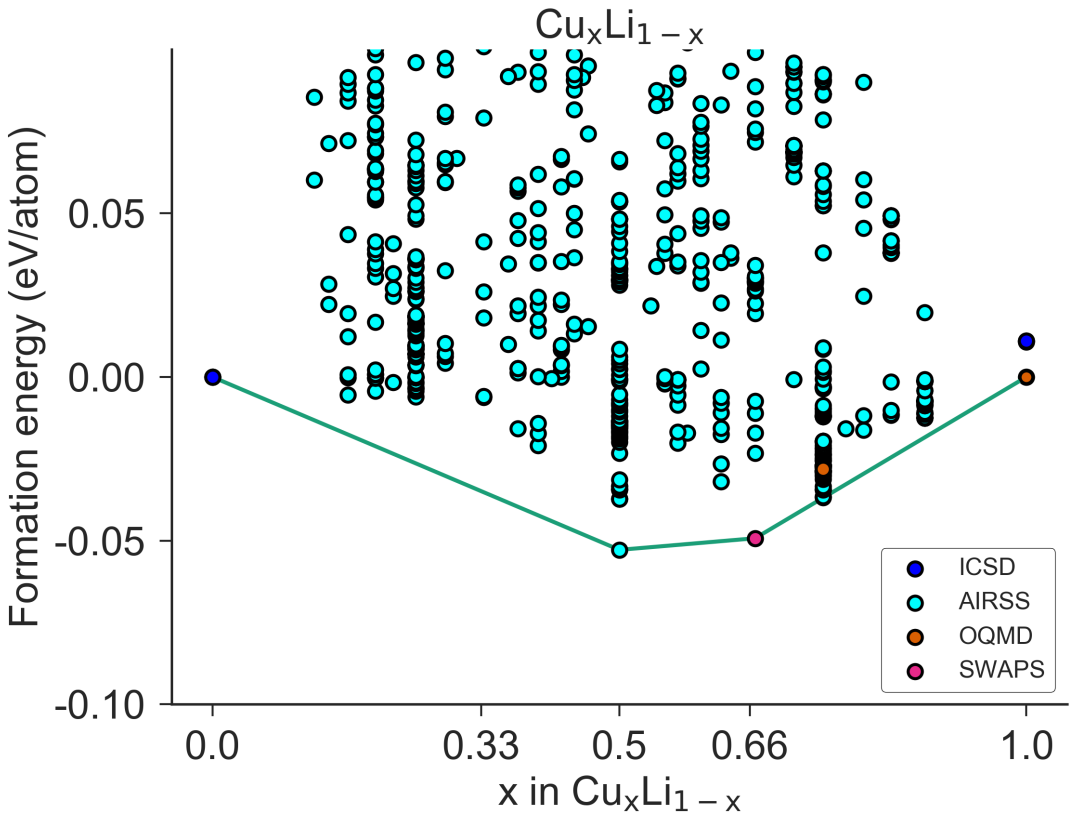

Fig. 3.4 Binary Cu-Li hull at 300 eV cutoff, 0.05 Monkhorst-Pack k-point spacing, with Vanderbilt ultrasoft pseudopotentials. Points represent structures on the phase diagram and are coloured by method used to identify the structure.

with Cu, because it would then no longer be a usable ion in the intercalation reaction with graphite, and could decrease conductivity of the Cu current collector.

The only experimentally identified structures Cu_4Li and Cu_2Li_3 are not on the convex hull tie-line in Figure 3.5, as they are destabilised by the low energy Cu_2Li and CuLi structures. Given that the pseudopotentials I have chosen are accurate only to within 10 meV/atom, this highlights the need to increase the energy cutoff and decrease the k-point grid spacing to converge the energy further to ensure that these ground state energies are correct. Clearly these results are highly dependent on the choice of functional, level of theory, and type of calculation done to determine the ground-state structures of Cu-Li. Further work is needed to calculate finite temperature profiles and pressure dependence of these structures in order to construct a full phase diagram and determine which of the structures suggested by the literature and by AIRSS are actually synthesisable.

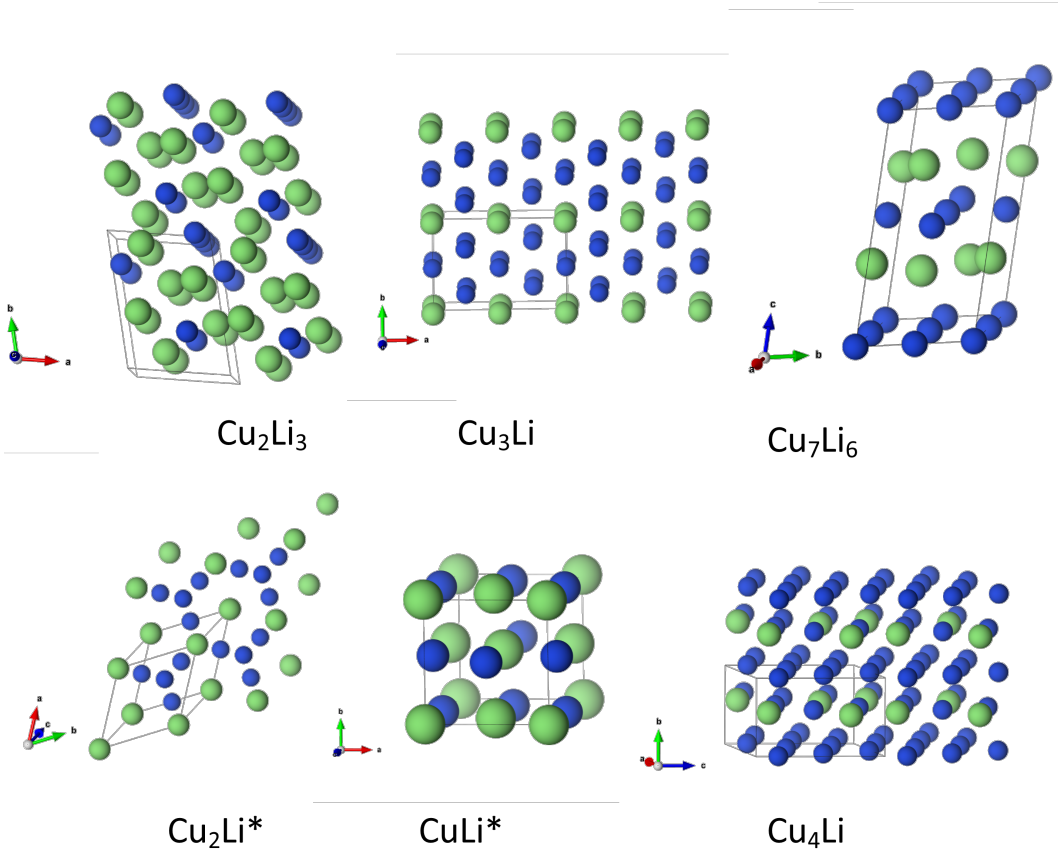

Fig. 3.5 Cu-Li binary structures from Table 3.2. Li coloured green, Cu in blue. Those structures which have an asterisk (*) are on the hull in Figure 3.5.

Material	Space Group	No. f.u.	Vol/f.u. (Å^3)	Hull dist. (meV/atom)	Literature
Cu_4Li_1	Pm	2	57.11	23.3	[73, 74, 70]
Cu_3Li_1	$I4/mmm$	2	45.52	0.8	[22, 9]
Cu_2Li_1 *	$Fd\bar{3}m$	2	39.25	0.00	[23]
Cu_7Li_6	$C2/m$	1	174.5	25.8	[23]
Cu_1Li_1 *	$I4_1/amd$	4	24.45	0.00	
Cu_2Li_3	Pm	2	72.5	21.4	[71, 75]

Table 3.2 Selected structures from the CuLi hull, both on the hull and those referenced by other works which were found using AIRSS. The structures with an asterisk (*) are those on the hull. Each structure is the lowest in energy for that stoichiometry.

3.3 Computational electrochemistry analysis

From the above Cu-Li phases as well as the Li-P phases from Mayo *et al.* and ternary phases from the OQMD, a ternary hull shown in Figure 3.6 is constructed which shows the gravimetric capacities of the structures as well as their relative distances from the 3D convex hull [25, 9].

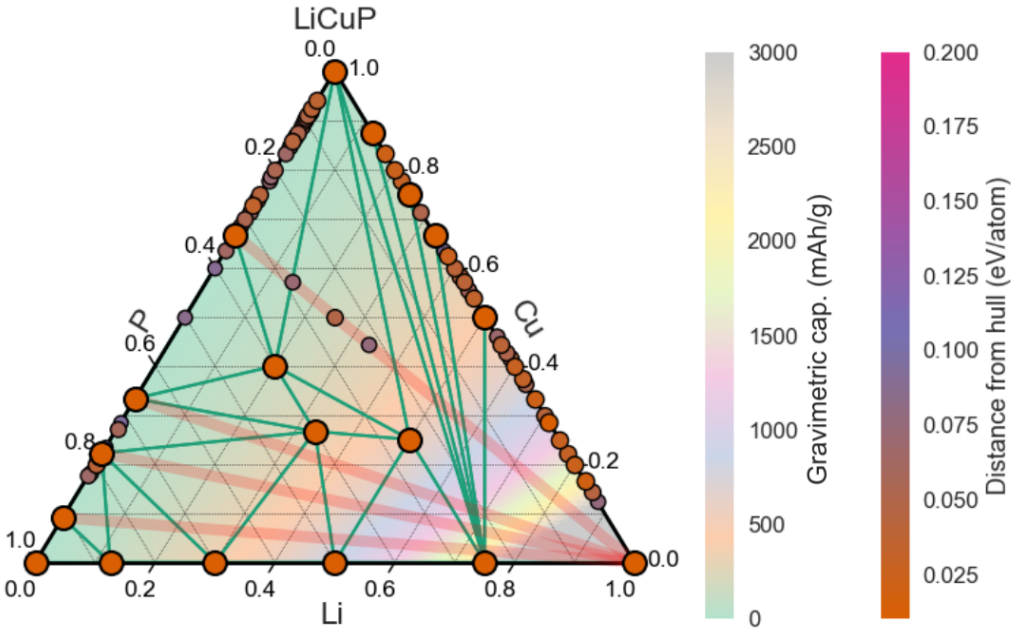

Fig. 3.6 Ternary hull between Li-Cu-P with points coloured and sized by hull distance with larger points closer to the hull, pathways from binary Cu-P structures to Li coloured in red, and ternary hull coloured by gravimetric capacity of resulting structures. Structures on the hull are shown as large orange points, with green tie-lines connecting the hull structures.

Voltage profiles were constructed between Cu-P and Li using the formation energies of structures on the tie-line in the ternary hull (Figure 3.6). The curves shown in Figure 3.7 represent the voltage profile between the binary Cu-P structures on the hull in Figure 3.2, the ternary phases (Cu_2LiP_2, $Cu_4Li_5P_6$, and $CuLi_2P$) found in the OQMD between Li-Cu-P, and the final products of Li_3P + CuLi, as laid out in Figure 3.6. Full details of the chemical reactions possible at each step of the voltage profile are shown in Appendix A.

Of the ternary phases found in the ICSD, $P6_3/mmc$ Li_2CuP and P-3m1 $LiCu_2P$ were identified as byproducts in cycling Cu_3P [12]. Another ternary phase $Li_{1.75}Cu_{1.25}P_2$ (a similar stoichiometry to $Cu_4Li_5P_6$) was cycled with Li but not included in this ternary phase diagram [17]. A full AIRSS search is needed to determine all the phases of Li-Cu-P which form during cycling, especially because experimental studies show large capacity fading, which could be attributed to side reactions with other ternary phases or incomplete reversed reactions.

Cu_2P has the highest Cu content, and thus has the lowest final gravimetric capacity of 847 mAh/g given that Cu offers no usable capacity towards the overall reaction. CuP_{10} on the other hand, has the highest final gravimetric capacity of 2226 mAh/g. Unlike the other copper phosphides, CuP_{10} is a polyphosphide which requires more extreme conditions for synthesis. Lange *et al.* used CuI, Cu_3P and red P at 1023 K and 820 K to synthesise CuP_{10} and the final products were thin needle-shaped crystals [20]. While the synthesis procedure is not as simple as the ball-milling method generally used for Cu-P synthesis, it is possible that the

large improvement in capacity may be worth the difficult synthesis process if indeed it could be encapsulated and cycled with Li.

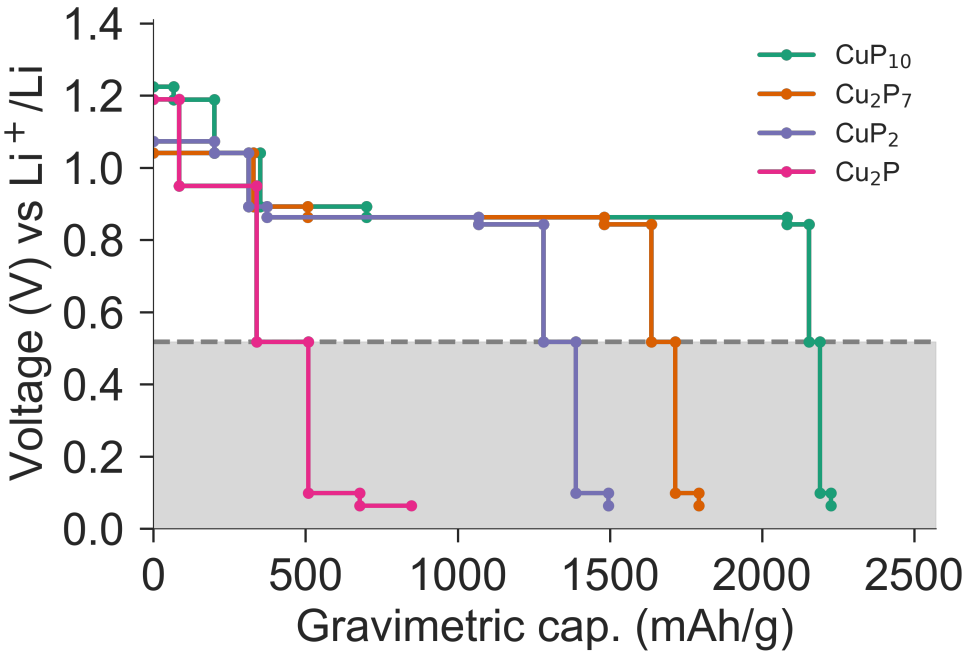

Fig. 3.7 Voltage profile of structures from Cu-P hull at 0 K. Ternary structures are from the known phases of Li-Cu-P from the OQMD database [9]. The grey region includes reactions with the CuLi phase, and the dashed line is the maximum capacity possible without including CuLi. Capacities within this grey region are only accessible through the addition of CuLi.

Section 3.2 suggests that the Cu-Li phases may not actually form during cycling. Thus, making the assumption that Cu-Li phases do not form, we can construct a voltage profile excluding these phases (see Figure 3.7 above grey region). By excluding the Cu-Li phases, the reactions now proceed as in equation 1.1 in which the final products are Cu + Li_3P. Assuming CuLi is inaccessible during cycling, the Li content in CuLi will not contribute to the overall gravimetric capacity, and the reactions will proceed until the grey dashed line shown in Figure 3.7, where Li_3P and Cu are formed. Without CuLi, the overall gravimetric capacities of each Cu-P phase would be decreased. In this case Cu_2P has a capacity of 508 mAh/g and CuP_{10} has a capacity of 2153 mAh/g.

To determine which voltage profile is more chemically relevant, it is useful to consider the experimental results of Wang *et al.*, in which they reacted CuP_2 in a Li cell [17]. While repeated cycling of the cell greatly reduced the overall capacity to around 360 mAh/g, the initial discharge of the cell exhibited a capacity of 1325 mAh/g. This is significant, as the theoretical capacity of CuP_2 with CuLi is 1495 mAh/g (Figure 3.7), while without CuLi is 1281 mAh/g (Figure 3.7 within shaded grey region). However the CuP_2 in experiment had a reversible capacity of 750 mAh/g after several cycles, which is well within the theoretical limit.

There are several possible causes for this initial high capacity, one potentially being the presence of Cu-Li structures. However, the Cu-Li phases form at low voltages (see Appendix A),

and there are several other possible causes for the initial high capacity, such as side reactions occurring, formation of a solid electrolyte interphase layer (SEI), or oxidation of the Cu in the anode. Within the experimental cell, reactions could be occurring between the anode and environment, or electrolyte, which I have not taken into account in these calculations. The formation of the SEI layer, while not fully understood, is known to cause some initial added capacity specifically from metal oxides forming between the liquid electrolyte and Cu-anode [76]. This could also explain the capacity loss observed by Wang and coworkers in [17], as the SEI layer is known to cause irreversible capacity fading. Finally the oxidation of Cu, either from the electrolyte or from an external source, could have caused this extra capacity in the first cycle of CuP_2. Thus, while further temperature-dependent ternary voltage profiles, as well as experimental studies need to be conducted to confirm this discrepancy, these initial calculations offer another source of extra capacity for CuP_2 which has not yet been considered in experiment.

While Cu_3P is the most widely used battery anode, from my analysis it was not on the convex hull tie-line, and thus the reaction pathway for Cu_3P was not shown. Additionally, while Cu_2P has moderately high capacity relative to graphite, and thus could be a stable anode material, it has not been identified experimentally. These results suggest a further analysis of both Cu_2P and Cu_3P to identify the ground-state of Cu_3P, which exists as a substoichiometric compound $Cu_{3-x}P$, and the possible reasons why Cu_2P has not yet been observed in cycling or synthesis experiments.

3.4 Electronic and structural analysis of Cu_2P and Cu_3P

A 2016, Yang *et al.* described the electronic structure of a 2D Cu_2P non-magnetic sheet, and suggested this structure could be a practical experimental 2D material [65]. While bulk Cu_2P, identified by AIRSS, was also found to lie on the hull, it has not yet been experimentally identified, despite being the closest stoichiometry on the convex hull tie-line to Cu_3P. Chemical synthesis of Cu_3P via ball-milling, most often produces $Cu_{3-x}P$ and CuP_2 [12, 14, 15]. While one would expect the ground-state structures on the convex hull to be formed via some synthesis route clearly this is not the case in this system, and thus these two structures are studied in more detail here, to determine what additional approximations may destabilise Cu_2P and stabilise Cu_3P, creating a ground-state picture which matches the experimental one.

3.4.1 Cu_2P

Yang identified a 2D layer of Cu_2P as a structurally strained semimetal in a single layer [65]. While Yang, *et al.* describe a 2D material, the convex hull in Figure 3.2 shows that the bulk Cu_2P structure is also energetically stable, given that it is on the tie-line of this hull. To assess the lattice stability of Cu_2P, phonon calculations at 500 eV and 0.03 k-point spacing were carried

out and are shown in Figure 3.8a. The fact that there are no imaginary phonon modes suggests Cu_2P is stable at least in the static lattice; the presence of such modes would suggest that the structure is stabilised by a shift in the atoms, meaning that in reality the lowest energy structure is of a slightly different space group. This indicates that phonons alone cannot explain why Cu_2P is not formed during battery cycling or as a by-product of Cu_3P. However, the stability of the phonons shown in Figure 3.8 suggest that it is possible to synthesise Cu_2P under a proper set of conditions.

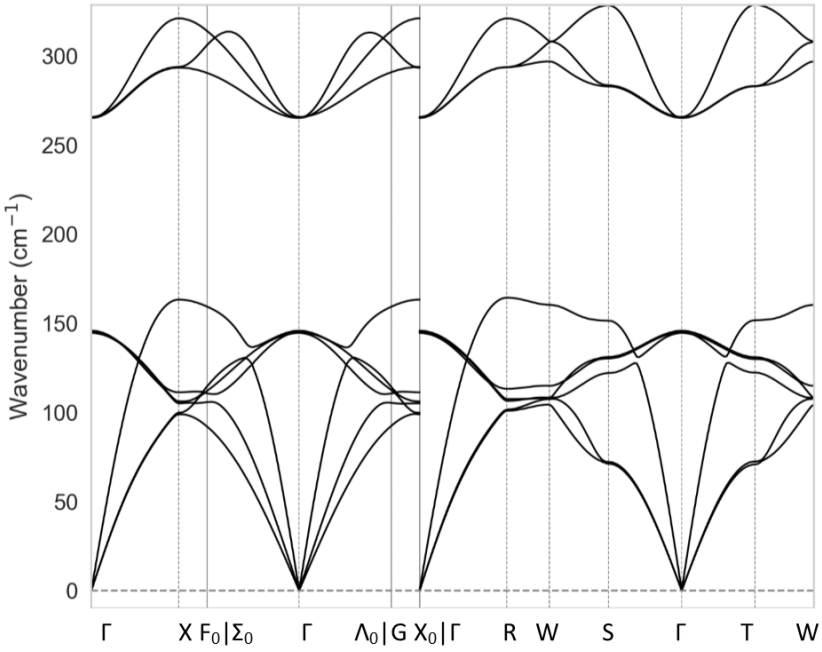

Fig. 3.8 a) Phonon modes of Cu_2P structure at 500 eV cutoff and 0.03 2πÅ^{-1} Monkhorst-Pack k-point spacing. There are no imaginary modes, suggesting this structure is stable at the static lattice level.

By studying the electronic structure of Cu_2P, we can understand the conductivity of Cu_2P as a possible anode material. As electrons flow into the anode after discharge, they will recombine with the anode structure and Li^+. An analysis of the Cu_2P band structure in Figure 3.9a shows that Cu_2P is metallic, given that the Fermi level resides within the bands, and is likely a semimetal from the fact that this Fermi level is below a gap in the band structure. Most transition metal phosphides are metallic, and Cu is a non-magnetic material, so we would expect Cu_2P to be metallic and non-magnetic. Additionally, there is very little spin-orbit interaction in this material, as shown in the spin-orbit coupled band structure in Figure 3.9c, where only a few bands below the Fermi level split at the gamma point. In the non-spin-orbit coupled diagram, most of the band character below the Fermi level is a contribution from Cu-d states, while just above the gap, the DOS shows a combination of both Cu-*s* and P-*s* states. Visualising this at the gamma point gives the orbital image shown in Figure 3.9a, which shows a negative orbital region around the P atoms, with a puckered cube-like positive region in

the 3D hexagonal void between Cu and P atoms. The 2D structure would not have had the space for such a positive region in one layer, but this could explain why the 2D structure has a buckled ground-state, given that the bulk AIRSS structure is stabilised with this charge region between atoms. Furthermore, this structure likely has the ability to hold an extra electron in its ground-state, possibly within the positive region between atoms shown in yellow in Figure 3.9a, moving the Fermi level up to the bottom of the gap in the band structure (as shown in Figure 3.9b) which suggests this material could transition from a semimetal to metal with doping. Given that during battery cycling, it is likely that parts of the anode bulk will take on extra charge, some areas of Cu_2P could be semiconducting as the electrons will be trapped in the unoccupied states in the valence band, thus lowering charge transport within the anode material.

Finally, we can compare the bulk structure of Cu_2P to similar known compounds including the computationally identified 2D structure from Yang [65]. The 2D Cu_2P is a non-magnetic in plane structure, however the AIRSS performed here is more likely to find fully connected 3D structures than 2D layers, and thus identified an *I*mma (close to *F*m$\bar{3}$m) 3D structure which has in-plane layers of copper and phosphorus. Both the 2D structure in Ref. [65] and the AIRSS Cu_2P structure have hexagonal symmetry in the layers. One major difference between the 2D structure and the AIRSS bulk Cu_2P is the phosphorus coordination. In the AIRSS bulk structure, phosphorous is 9-fold coordinated whereas the 2D structure is 6-fold coordinated. While phosphorus is known for having high coordination, 9-fold coordinated phosphorus is only found in two other structures of M_2P, which are Ir_2P and Rh_2P. Though Cu is a first-row transition metal, the Cu_2P structure resembles that of both Ir_2P and Rh_2P, in that both are *I*4/mmm (a symmetrically similar space group) and have 9-fold coordinated phosphorus atoms in the structure. Both of these materials have been synthesised under high temperatures and pressures suggesting a possible synthesis route for Cu_2P [77]. However, the extreme conditions needed to synthesise the Rh and Ir compounds could explain why Cu_2P has not yet been identified as a by-product of other copper phosphides, and may need to be specifically synthesised in a targeted way, under such extreme conditions as Rh or Ir compounds.

3.4.2 Cu_2P + Li

While several ternary phases of Cu-Li-P are already known, given the limited knowledge of Cu_2P there is potential for related ternary structures, which have not yet been identified, to form. By using AIRSS to randomly add one, two, or three, Li to the Cu_2P structure, three structures were identified within 0.1 eV/atom of the ternary hull between Cu-P-Li. Though each structure is above the ternary hull tie-lines, they all are lower in formation energy than Cu_2P suggesting that the addition of Li is locally stabilising to Cu_2P but not in the full context of the ternary hull. The presence of these metastable structures is further significant, as it suggests this part of the hull should be further searched beyond just lithiating Cu_2P to find

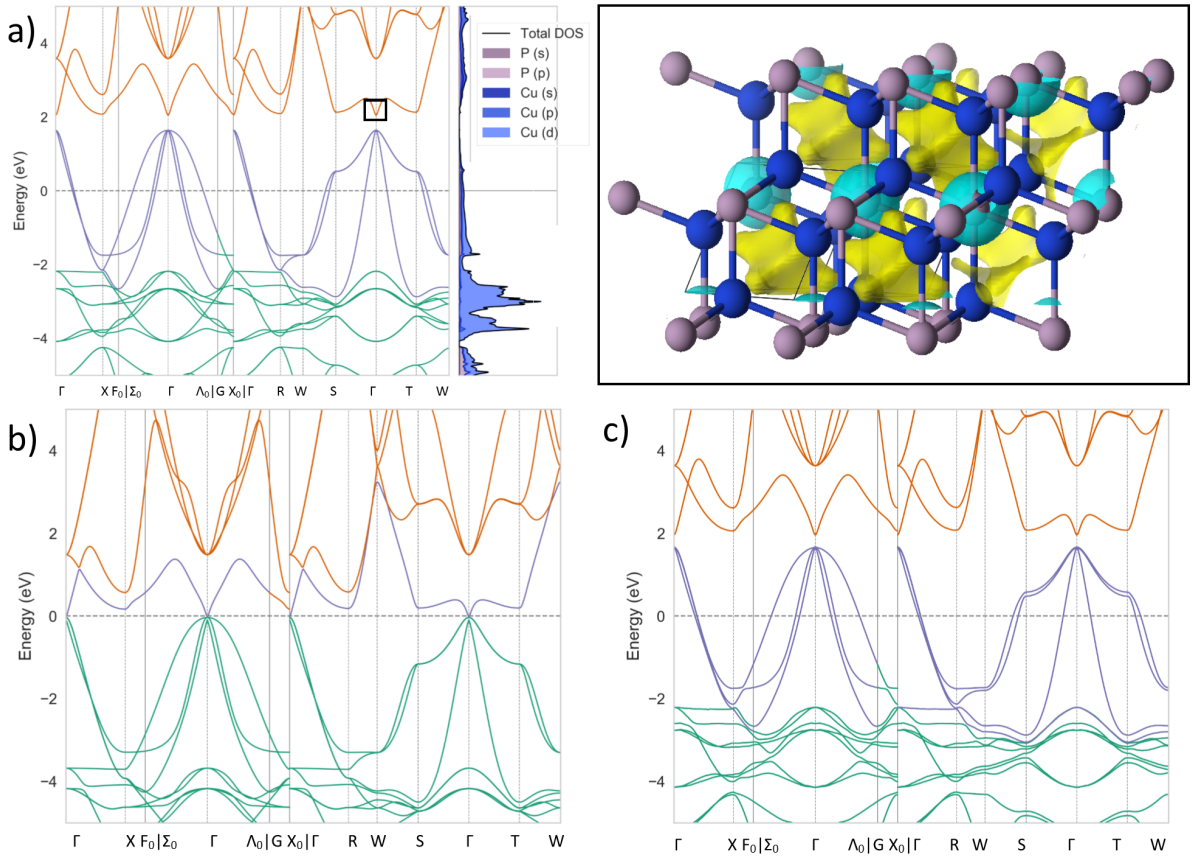

Fig. 3.9 a) Band structure of Cu_2P without spin-orbit coupling. The bands in each figure are coloured orange above the Fermi level, green below, and purple if the bands cross or touch the Fermi level. Image of orbitals defined by the band above the Fermi-level at the gamma point in the band structure shown on right. In the structure, P is coloured pink, Cu is blue, with positive isosurfaces in yellow and negative in cyan. The boxed area on the band structure plot shows the area where the orbitals are being calculated. b) Band structure of Cu_2P without spin-orbit coupling and with one electron added. c) Band structure including spin-orbit coupling showing the splitting of the bands. Compare this to the band structure in a) which does not include band splitting from spin-orbit coupling.

other copper phosphides in this stoichiometry region. The structures intercalated with Li, are shown in Table 3.3 with images of each structure shown in Figure 3.10. As subsequent Li atoms are added to the unit cell, the bonds between Cu and P are broken, and voids are created between these CuP chains to host the Li atoms.

Mauvernay, *et al.* suggested in 2005 that during Li insertion in Cu_3P an amorphous phase, $LiCu_2P$ was formed, but were unable to confirm this phase using XRD [12]. Given that $LiCu_2P$ is only 50 meV from the hull at 0 K, and is amorphous this could suggest that at finite temperature this phase, or a similar phase does form, as previous studies have formed metastable phases 40 meV/atom above the hull during cycling [78]. A finite temperature ternary hull would need to

be constructed in order to confirm its existence, and further *in situ* XRD measurements are needed to confirm this $LiCu_2P$ phase.

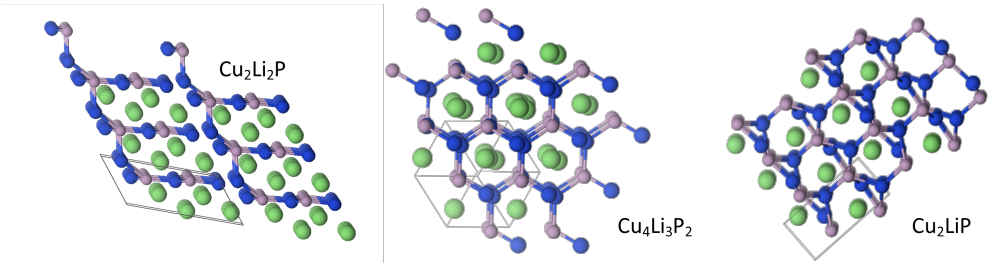

Fig. 3.10 Three lowest energy structures from Table 3.3 obtained by lithiating the Cu_2P structure from AIRSS with one to 4 Li per unit cell. The Li preferentially sits between hexagonal structures of Cu and P, while breaking down the initial Cu_2P structure. The atoms in this figure are coloured as follows: P in pink, Li in green, Cu in blue.

Material	Space Group	No. f.u.	Vol/f.u. ($Å^3$)	ΔE vs Ternary (meV/atom)	ΔE vs. Cu_2P (meV/atom)
$Cu_2Li_1P_1$	$P1$	2	49.6	46.5	-221
$Cu_4Li_3P_2$	$P1$	1	114.3	77.9	-265
$Cu_2Li_2P_1$	$P1$	2	62.9	125.0	-279

Table 3.3 Structures from lithiating Cu_2P AIRSS search ordered by the number of Li per Cu_2P structure added to the cell. Each are above the hull tie-line, but negative in formation energy relative to Cu_2P.

3.4.3 $Cu_{3-x}P$

The theoretical existence of Cu_2P is the reason that neither Cu_3P nor one of its substoichiometric counterparts was on the hull at the static lattice level, since Cu_2P was lower in formation energy, thus lowering the hull tie-lines. It is well known that Cu_3P as synthesised, is closer to $Cu_{3-x}P$ and contains Cu vacancies within the $P6_3cm$ structure [68, 62]. However, the nature of these vacancies is somewhat disputed. The original structure solution by Oloffson *et al.*, synthesised using a heating and quenching method, suggested that the stoichiometry was between $Cu_{2.82}P$ and $Cu_{2.73}P$ at 700 ^oC, and the vacancies are present at the 6c copper sites [62]. The ICSD structure of Cu_3P is the $P6_3cm$ space group. This structure is 56.0 meV/atom above the convex hull, and as such is not energetically stable at the static lattice level. Given that $Cu_{3-x}P$ is experimentally observed, there should be another structure that lies near the convex hull tie-line in formation enthalpy per atom and has structural similarity to the space group of Oloffson's Cu_3P, but with vacancies on the Cu atoms as Oloffson suggested. The lowest energy structures, from this AIRSS search, of $Cu_{3-x}P$ are shown in Table 3.4.

DFT calculations from De Trizio *et al.* [68] have suggested the vacancies in Cu_3P are present at the 6c Wyckoff sites, which they denote "Cu2". From the calculations in this work, the $Cu_{17}P_6$ structure has one vacancy at the "Cu2" site shown in Figure 3.11, and Cu_8P_3 has two vacancies at Cu2 sites. However their calculations showed that there was one vacancy at a Cu1 site, and another at a Cu2 site. Both Cu1 and Cu2 are in the 6c Wykoff site. In the structure from De Trizio, the vacancies were introduced by first removing one atom from the Cu_3P structure to obtain $Cu_{17}P_6$, and then removing a second Cu atom, forming Cu_8P_3, thus limiting the number of vacancies possible for the Cu_8P_3 structure. Given that our structures were not dependent on one another, we have a vacancy in the lowest energy $Cu_{17}P_6$ structure (Figure 3.11 vacancy coloured black), which is not present in the Cu_8P_3 structure. This suggests that the overall ground-state $Cu_{3-x}P$ could have one of many possibly vacancy orderings, or a combination of those found in this paper as well as in [68], given that both are energetically favourable, though from our calculations neither is on the convex hull tie-line. DFT is aimed at finding the lowest energy ground-state structure, and thus to find a composition which is stable over many different configurations in DFT would require an unrealistically large supercell, or many finite-temperature calculations. For such a case, it would be necessary in the future to possibly model this system using statistical mechanical methods such as cluster expansion which are aimed at calculating global properties of a material.

Material	Space Group	No. f.u.	Vol/f.u. (Å^3)	Hull dist. (meV/atom)	Provenance
Cu_3P_1	$P6_3cm$	6	48.2	56.0	ICSD
Cu_3P_1	$P1$	2	50.8	42.8	GA
$Cu_{17}P_6$	Cm	2	283.8	45.2	GA
Cu_8P_3	$P2_1$	2	138.7	32.0	AIRSS

Table 3.4 Lowest energy structures within 50 meV of convex hull with formula $Cu_{3-x}P$ where $x < 1$. There are two Cu_3P structures, one from the ICSD which is 56 meV above the convex hull and one from the GA which is only 42.8 meV above the convex hull, suggesting it is more stable.

3.5 Temperature and pressure effects on copper phosphides

Up to this point, the ground-state phases of Cu-P have been studied at static lattice and 0 GPa. However, Li-ion batteries especially in portable electronic applications are subjected to more extreme conditions than these theoretical calculations have yet accounted for. Battery cycling can cause both elevated temperatures and pressures which can alter the structure of materials in the anode, and further change the voltage profile and performance of the battery material [79].

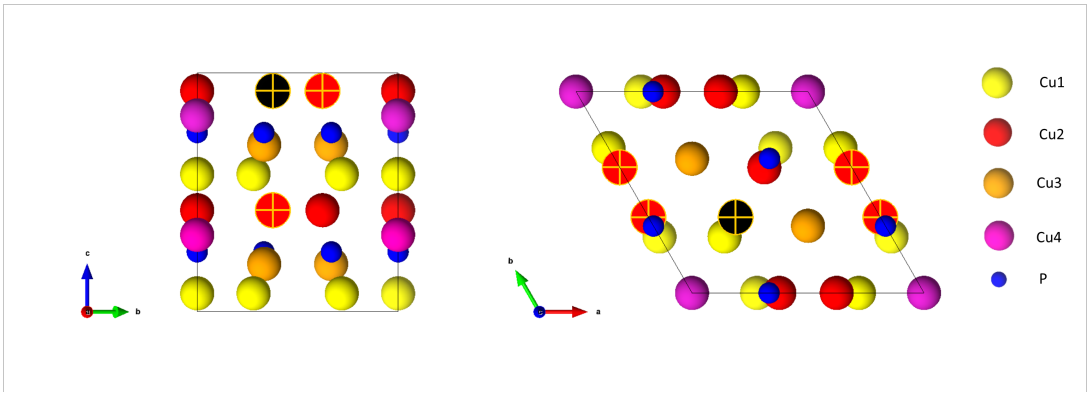

Fig. 3.11 The ICSD structure of Cu_3P as identified by Oloffson, with the vacancies denoted by yellow crosses on the Cu2 sites shown here. These colours and the Cu1, Cu2, Cu3, and Cu4 sites are chosen for direct comparison to [68]. The black atom is the single vacancy in $Cu_{17}P_6$, and should be coloured red otherwise but is black to be visible to the reader as different from the two red vacancies which are present in Cu_8P_3.

3.5.1 Pressure dependent convex hull of Cu-P

In 1998, Goryachev proposed a pressure-dependent phase diagram of Cu-P, which predicted that CuP was stable at pressures of 100 GPa [80]. While a battery would likely not reach such extreme pressures, we tested a moderate application of 10 GPa hydrostatic pressure, as well as 100 GPa on 450 structures closest to the convex hull at 0 GPa. These structures were generated from the initial AIRSS search at 0 GPa and another high-pressure AIRSS search was not performed. From the hull shown in Figure 3.12a, CuP is not stable at 10 GPa, but Cu_2P, CuP_2, and CuP_9 are. Interestingly, CuP_{10} is no longer on the tie-line between lowest energy structures, but has been replaced by CuP_9 which previously was 182 meV/atom above the hull in energy at 0 GPa.

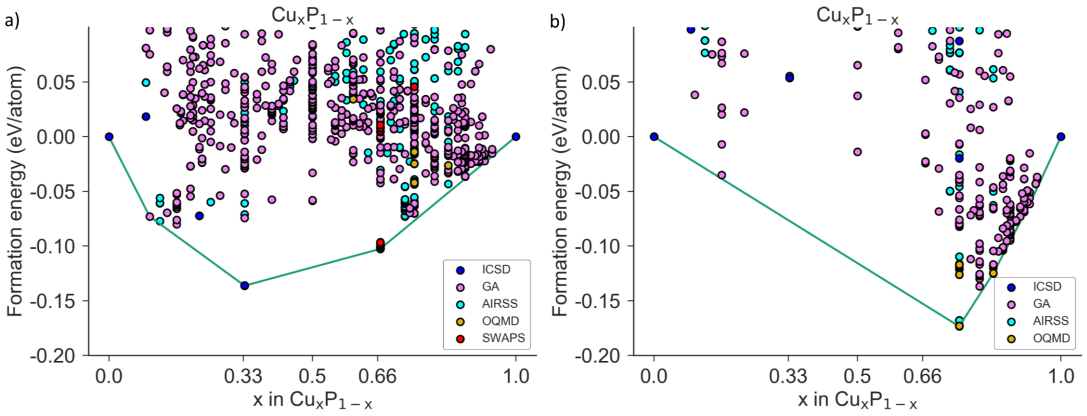

Fig. 3.12 a) Convex hull of structures at 10 GPa between Cu and P. Geometry optimised at 300 eV cutoff, 0.05 2π Å^{-1} Monkhorst-Pack k-point spacing, with Vanderbilt ultrasoft pseudopotentials. Points labelled by method used to identify structure at 0 GPa. b) Convex hull of structures at 100 GPa between Cu and P. Geometry optimised at the same accuracy as panel a.

Material	Parent Structure	Space Group	No. f.u.	Vol/f.u. (Å^3)	Hull dist. (meV/atom)	Provenance
$Cu_{16}P_1$	$Cu_{12}P$	$P1$	1	184.17	2.69	GA
$Cu_{12}P_1$	$Cu_{12}P$	$P1$	1	140.77	1.54	GA
$Cu_{11}P_1$	$Cu_{12}P$	$P1$	1	130.02	8.78	GA
$Cu_{10}P_1$	$Cu_{12}P$	$P1$	1	119.30	5.17	GA
$Cu_{19}P_2$	$Cu_{12}P$	$P1$	1	228.56	13.24	GA
Cu_9P_1	$Cu_{12}P$	$P1$	1	108.46	7.79	GA
Cu_8P_1	$Cu_{12}P$	$P1$	1	97.93	9.52	GA
Cu_7P_1	Cu_7P	$P4/mbm$	2	87.09	2.00	AIRSS
$Cu_{13}P_2$	$Cu_{12}P$	$P1$	1	164.06	11.73	GA
Cu_6P_1	$Cu_{12}P$	$P1$	1	76.26	12.14	GA
Cu_5P_1	Cu_7P	$Pmn2_1$	2	65.47	8.04	AIRSS
Cu_3P_1	Cu_3P_1	$P1$	6	45.56	6.80	GA
$Cu_{17}P_6$	Cu_3P_1	Cm	1	267.50	10.66	GA
Cu_8P_3	Cu_3P_1	$P2_1$	2	130.49	10.97	AIRSS
Cu_2P_1 *	Cu_2P_1	$P\bar{1}$	2	37.19	0.00	GA
Cu_1P_2 *	Cu_1P_2	$P\bar{1}$	4	43.08	0.00	GA
Cu_1P_5	Cu_1P_7	$P1$	6	78.41	10.97	GA
Cu_1P_6	Cu_1P_7	$P1$	1	93.27	15.11	GA
Cu_1P_7	Cu_1P_7	$Pba2$	2	104.30	2.48	AIRSS
Cu_1P_9 *	Cu_1P_7	$P1$	1	131.45	0.00	GA

Table 3.5 Lowest energy structures within 20 meV of convex hull at 10 GPa. Here formula unit is f.u. and structures on the hull are denoted by an asterisk (*). Parent structure refers to the most similar structure in visual comparison to that structure, suggesting that the structure in the table is derived from its "parent structure". These groups are shown in Figure 3.13

Many of the Cu-rich structures are stabilised by this moderate application of 10 GPa hydrostatic pressure, including the ICSD structure, Cu_3P, which is now only 7 meV/atom from the convex hull, whereas the Cu-deficient structures Cu_8P_3 and $Cu_{17}P_6$ are 10 meV/atom above the hull (see Table 3.5. The CuP_2 structure now lowest in energy is a GA-identified $P\bar{1}$ structure, and many of the structures such as Cu_2P which had higher symmetry at 0 GPa are now $P1$ or $P\bar{1}$ space group. While Cu_2P and CuP_2 had similar structures at 10 GPa, with 2% bond length shortening, the 10 GPa structure of CuP_9 shared little similarity to the CuP_{10} structure at 0 GPa.

All of these structures that are $P1$ or $P\bar{1}$ are identified by the GA, and by performing a visual analysis of these GA structures in relation to the AIRSS or ICSD structures identified within 20 meV of the tie-line. A cutoff of 20 meV was chosen to limit the large quantity of structures which would be present in a higher cutoff energy. We can characterise the structures into four main groups: CuP_7-like, Cu_8P_3-like, Cu_5P-like, and what here I will call CuP_{12}-like although $Cu_{12}P$ is still $P1$ space group. Figure 3.13 shows the general structure of these groups. In

addition, Cu_2P and CuP_2 are distinct from many of these structures and thus are not separated into a group. The parent structure column in Table 3.5, identifies which group each structure belongs to.

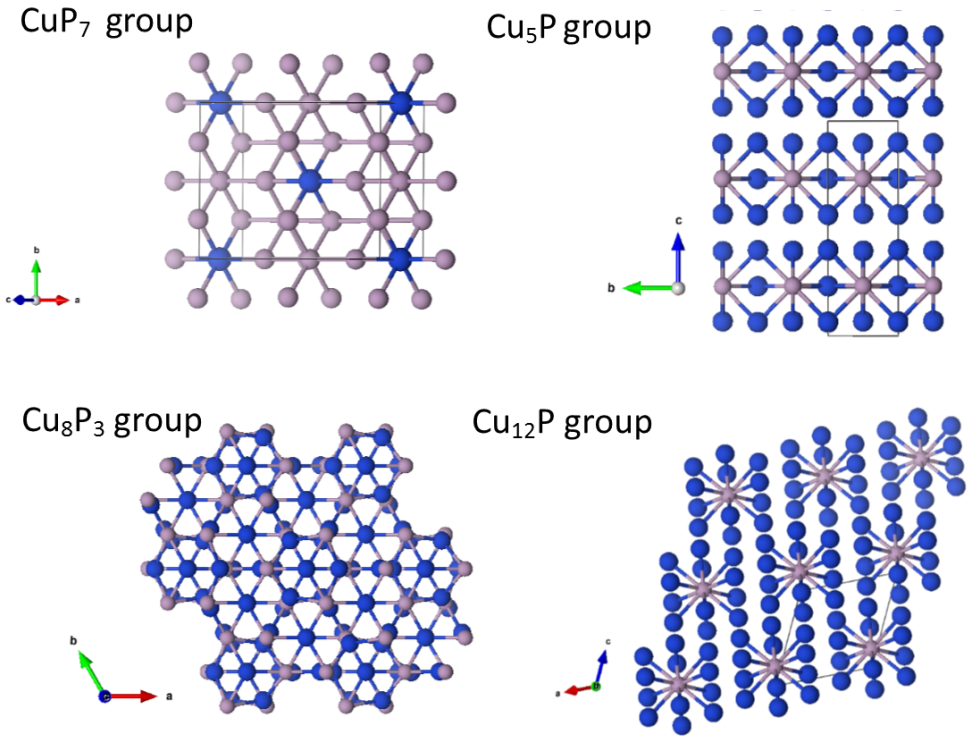

Fig. 3.13 Representative structures from the four visual classifications of the Cu-P structures at 10 GPa. CuP_7 is *P*ba2, Cu_5P is *P*mn2$_1$, Cu_8P_3 is *P*2/1, and $Cu_{12}P$ is *P*1.

At 100 GPa, most structures are in the $Cu_{12}P$ group, and have high phosphorous coordination and high density. While CuP is not on this hull, as Goryachev had predicted [80], it is clear from these initial results showing many pressure-stabilised structures that further AIRSS searches are necessary in order to confirm the presence of these structures at 10 and 100 GPa. However, it is possible that some of the copper phosphides at 100 GPa do form, given that many metallophosphides are known to have upwards of 9-fold coordination, and many of these structures are between 6 and 9-fold coordinated. The hexagonal and six-coordinated phosphorus, in the $Cu_{12}P$ group are clearly stabilised by pressure as at 100 GPa almost all structures have some hexagonal symmetry. Finally, the Cu_3P structure on the hull at 100 GPa is a swap from Al_3Sb, a metal alloy with *I*4/mmm space group. It has a similar structure to those in the Cu_8P_3 group, with slightly elongated hexagons in the a* direction. While these initial results suggest several stable structures at high pressure, a further search could confirm these phases.

Material	Parent Structure	Space Group	No. f.u.	Vol/f.u. (Å^3)	Hull dist. (meV/atom)	Provenance
$Cu_{16}P_1$	$Cu_{12}P$	*P*1	1	145.42	10.31	GA
$Cu_{15}P_1$	$Cu_{12}P$	*P*1	1	136.86	7.04	GA
$Cu_{12}P_1$	$Cu_{12}P$	*P*1	1	111.30	10.99	GA
$Cu_{11}P_1$	$Cu_{12}P$	*P*1	1	102.66	17.11	GA
$Cu_{10}P_1$	$Cu_{12}P$	*P*1	1	94.25	15.31	GA
Cu_9P_1	$Cu_{12}P$	*P*1	1	85.69	12.16	GA
Cu_8P_1	$Cu_{12}P$	*P*1	1	77.04	8.12	GA
Cu_7P_1	$Cu_{12}P$	*P-1*	2	68.65	9.56	GA
Cu_6P_1	$Cu_{12}P$	*P*1	1	60.02	5.47	GA
$Cu_{11}P_2$	$Cu_{12}P$	*P*1	1	111.41	11.27	GA
Cu_5P_1 *	Cu_5P	*Amm2*	1	51.43	0.50	OQMD
Cu_4P_1	Cu_5P	*P*1	1	42.92	18.76	GA
Cu_3P_1 *	Cu_8P_3	*R3m*	1	34.55	0.32	OQMD
Cu_1P_5 *	Cu_2P_7	*P*1	1	54.92	0.00	GA

Table 3.6 Lowest energy structures within 20 meV of convex hull at 100 GPa. Here formula unit is abbreviated as f.u. and structures on the hull are denoted by an asterisk (*). The parent structures are shown in Figure 3.13 and are the same groups as at 10 GPa.

3.5.2 Temperature dependent convex hull of Cu-P

The final, and possibly most crucial piece connecting this theoretical work to real battery applications is the addition of temperature-dependent calculations. No battery will ever operate at 0 K, and thus it is important to understand how the energies of each structure change with the application of temperature. However, Figure 3.14 shows that while Cu_8P_3 is stabilised by around 20 meV/atom up to 1000 K, Cu_2P is also highly stable at this temperature and thus Cu_8P_3 does not cross the hull tie-line. Clearly, there are further effects taking place which neither DFT nor a Harmonic Approximation have accounted for yet.

The hull in Figure 3.14 suggests that the crystals of both CuP_{10} and CuP_2 are destabilised at finite temperature, given that both of these structures exhibit an increase in free energy, while both Cu_2P and Cu_8P_3 are stabilised with respect to their initial static lattice free energy. However, the Cu_8P_3 structure is still not stable at finite temperature, up to 1000 K, given that Cu_2P is on the hull tie-line at this temperature, while Cu_8P_3 is not. Thus while the vacancies are energetically favoured, they do not explain fully why Cu_8P_3 forms instead of Cu_2P. Experiments have shown that after forming Cu_3P often CuP_2 is also formed as a by-product, thus we had expected that at finite temperature Cu_2P had a higher formation energy compared to at 0 K, while we find that higher temperatures are stabilising for both Cu_3P and Cu_2P. From Figure 3.14, Cu_2P is most stable at finite temperature, CuP_2 and Cu_3P are closer in formation energy at 1000

K than at 0 K. These results suggest that there may be a kinetic barrier, besides thermodynamic effects between Cu_2P and CuP_2 formation.

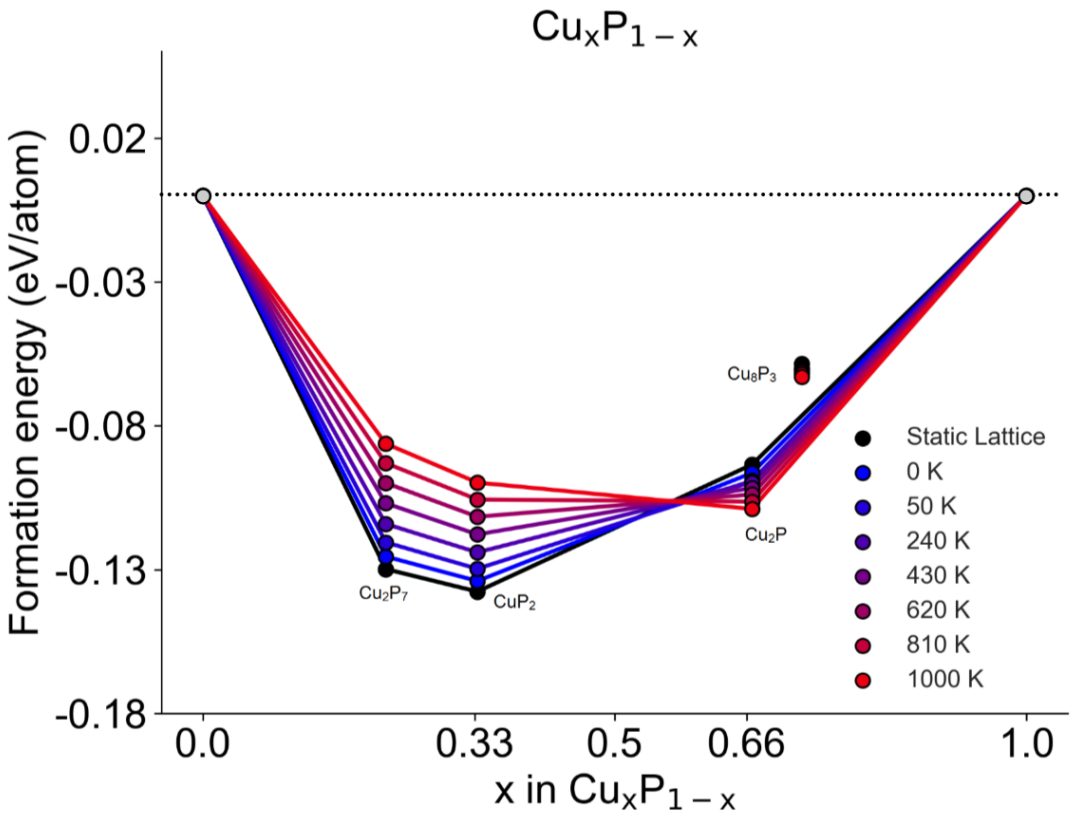

Fig. 3.14 Convex hull of structures plotted using E_f as Gibbs free energy from temperature dependent phonon calculations. The Cu and P chemical potentials (shown in grey) are also approximated at each temperature and the hull is then re-normalised to a formation energy of 0 eV/atom for those chemical potentials. The dashed line indicates the line of 0 E_f for reference.

3.6 Conclusions

This work on Cu-P and Cu-Li phase diagrams has provided several new insights into these systems, and put them in the context of Li-ion batteries. Within the copper phosphide system, it is clear that the experimentally known Cu_8P_3 phase is partially lowered in ground-state energy by temperature, but not to the extent that it would lie on the convex hull between Cu and P, and Cu_3P is stable in a $P\bar{1}$ phase at 100 GPa pressure. Cu_2P, on the other hand, is stable as a static lattice, at finite temperature, and at 10 GPa, but does not form during chemical synthesis of Cu_3P even as a side product of this reaction. It is also possible that Cu_2P could be destabilised by anharmonicity, and future calculations should consider this possibility for the Cu_2P finite temperature calculations. Additionally, band structure calculations show that Cu_2P has minimal spin-orbit coupling, is a semimetal with the Fermi energy below the band

gap, and becomes a semiconductor by doping with one electron. In the ternary phase diagram, a potential $LiCu_2P$ phase was identified by lithiating the Cu_2P structure, but further ternary searches are needed to find a phase which is on the hull, and finite temperature calculations to see if this phase is stabilised by temperature. Within the Cu-Li phase diagram, potential new phases of CuLi and Cu_2Li were formed, but given that the Cu-Li hull is only 50 meV deep and literature suggests there are large discrepancies between computation and experiment, these phases are not likely to be experimentally relevant. The ternary voltage profiles constructed both with and without these Cu-Li phases, could suggest that some Cu-Li phases may be found upon initial charging of the batteries, given that experimental results have shown a large initial capacity for CuP_2 which is higher than the theoretical capacity calculated without consideration of the Cu-Li binary phases. However, there are many other factors to include in assessing the source of this extra capacity, such as SEI formation, oxidation of Cu, and side reactions. Finally, of all the Cu-P binary structures, CuP_{10} showed the most promise, with a gravimetric capacity of 2153 mAh/g. While it may experience large volume expansion given its close relationship to P, the benefits of a high capacity may outweigh these expansion issues. These results suggest that CuP_{10} should be tested as a battery anode, given its high theoretical capacity, and that Cu_2P may be synthesiseable, though further calculations are needed to fully understand why it has not yet been identified, given that it is stabilised by both temperature and pressure.

Chapter 4

Iron phosphide anodes

While Cu-P anodes have been tested and implemented in Li-ion batteries, and the previous chapter suggests that CuP_{10} is a possibly higher capacity anode, neither Cu nor Li is earth-abundant. Substituting Cu for an earth-abundant element such as Fe (two to the left from Cu in the periodic table) and Li for Na provides an example of how similar elements may change the overall battery performance, and a comparison for the Li-ion battery case discussed in Chapter 3. Furthermore, the use of Na ions will eliminate the need for a Cu current collector (Al is used in Na-ion batteries), further reducing the cost of the battery. Overall, Fe-P shows promise as an anode in Na-ion batteries, as P has small volume expansion of around 23 $Å^3$/Na, and a high theoretical capacity of 2600 mAh/g [8, 81]. Additionally, in Li-ion batteries, FeP_2, FeP_4, and FeP have been tested and shown to have reversible capacities from 720 mAh/g for FeP to 530 mAh/g for FeP_4 after the second cycle [13, 82]. In Li-ion batteries FeP_4 is shown to have a reversible insertion mechanism which forms an unknown phase of fcc Li_xFeP_4. Reversibility is a key component of transitioning these anodes to Na-ion batteries, as the larger Na ions require more stable structures during cycling, so as not to degrade the anode after multiple cycles. In one instance, FeP_4 was successfully cycled in a Na-ion half-cell with a reversible capacity of 1100 mAh/g over 30 cycles, thus confirming that Fe-P is a good candidate for further research into Na-ion battery anodes [21]. Beyond the study in [21], there has not been extensive characterisation of the Na-Fe-P system experimentally or computationally, and no ternary phases have been described. The following sections describe a crystal structure search performed on both the Fe-P and Na-Fe-P systems, in the context of Na-ion anodes.

4.1 Spin polarisation in high throughput searching

Unlike Cu, bulk Fe is ferromagnetic. To treat this magnetic moment properly using DFT, it is necessary to take into account the spin components of the density. This can be done either through collinear spin polarisation, in which the total density is broken into spin up and spin down densities using the approximation,

$$\rho_{tot}(r) = \rho_{+}(r) + \rho_{-}(r); \tag{4.1}$$

or through non-collinear spin polarisation, which allows the spins to vary both up and down, as well as over angles θ and ϕ. The Local Spin Density Approximation (LSDA) is dependent only on the density of the system, whereas the approximations made using GGA (effectively a Generalised Spin Gradient Approximation GSGA) functionals with spin dependence are based upon both the spin density and the gradient of the spin density. The non-collinear approach is used to study more complex magnetic ground-state s, and as such here is not used to test the high-throughput spin symmetry breaking, but only would be implemented as a post-processing step [83]. Furthermore, calculations using collinear spin polarisation predict the ground-state magnetic moment of ferromagnetic bcc Fe to be 2.22 μ_B (equivalent to the experimental value of 2.22 μ_B). Using the collinear approximation for the different magnetic phases of Fe reproduces the experimentally determined ordering of the Fe magnetic phases from the ground-state ferromagnetic bcc-Fe to the highest energy non-magnetic bcc Fe. The phases are shown in table 4.1, and match previous theoretical results using GGA functionals and collinear spin treatment to determine the magnetic ordering of Fe [84].

Fe Type	Magnetic Ordering	μ_B	ΔE (eV/atom)
bcc	FM	2.22	0.0
fcc	AFM	2.65	0.073
fcc	NM	0.00	0.106
fcc	FM	2.89	0.106
bcc	NM	0.00	0.45

Table 4.1 Table detailing the ground-state energies and magnetic moments of bulk Fe for bcc and fcc phases determined using collinear spin polarisation. The magnetic orderings are described as ferromagnetic (FM), nonmagnetic (NM), and antiferromagnetic (AFM)

Accounting for a spin degree of freedom allows the number of up and down spin electrons to be unequal, but the resulting two sets of equations are solved in exactly the same self-consistent manner as described in Section 2.1. While this will change the electron densities and has a great effect on density of states calculations as well as band structure calculations, in the case of high-throughput searching, the quantities of interest are first the total enthalpy per atom for each structure, and then the formation energy with respect to the convex hull. It is thus the formation energy that becomes most important for these initial searches. For one spin-polarised geometry, it is possible to have more than one ground-state lowest energy configuration corresponding to a different spin symmetry. These different configurations are accessible in one of two ways: either by breaking the spin symmetry on specific atoms in the unit cell or by setting an initial spin symmetry for the entire unit cell. In the Li-FeS_2 system,

AIRSS searches were performed in which both atoms and the initial spins on each atom were randomised for each search, however, a rigorous method for searching with spin-polarisation has not yet been defined, and thus here we will briefly explore how this spin polarisation should be carried out in an AIRSS search [60].

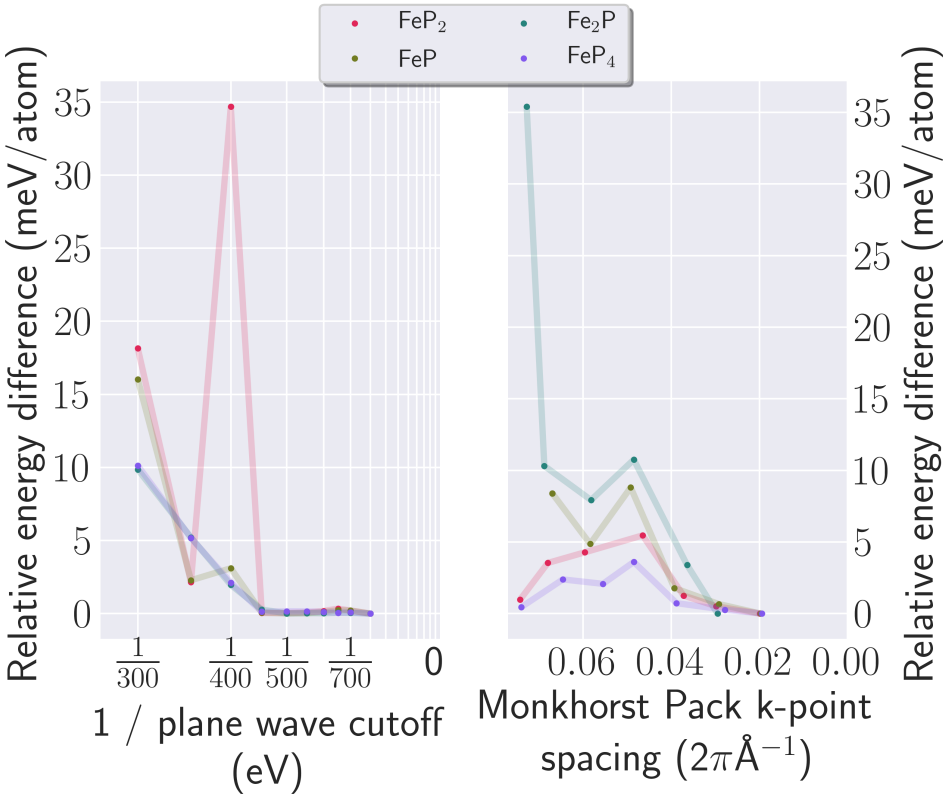

Fig. 4.1 These figures show the convergence of the energies of each ground-state Fe-P structure from the OQMD [9] with respect to the energy of the finest k-point highest energy cutoff criteria. Energies were calculated using a single-point calculation with the CASTEP QC5 ultrasoft pseudopotentials.

The CASTEP QC5 set of ultrasoft pseudopotentials was used for preliminary searching, as ultrasoft pseudopotentials have been shown to accurately reproduce spin configurations in Fe, Co, and Ni [85]. QC5 refers to the q_c parameter used in pseudopotential optimisation to minimise the kinetic energy below a certain threshold. These pseudopotentials are slightly "harder" than the set of Vanderbilt ultrasoft pseudopotentials used for the copper phosphide searches (thus requiring a larger plane wave energy cutoff), and in this case the q_c parameter is set to 5 for each pseudopotential. Figure 4.1 shows the convergence parameters for the QC5 set of pseudopotentials; from this a plane wave basis set energy cutoff of 450 eV and Monkhorst Pack k-point spacing of 0.05 2π Å^{-1} was chosen to sample the search space to energy differences within 10 meV/atom. From a set of 250 Fe-P compounds in the OQMD, and from structures of other transition-metal pnictides in the OQMD whose elements were substituted for Fe and P, these structures were geometry optimised in two ways, to determine which spin symmetry

breaking method should be used for an AIRSS search [9]. The first optimisation was carried out by breaking the spin symmetry first on the entire unit cell and the second, by breaking the spin symmetry on the first Fe atom in the unit cell by setting the spin to +5 on that specific Fe atom. A scatter plot of the resulting difference in formation energies is plotted in Figure 4.2.

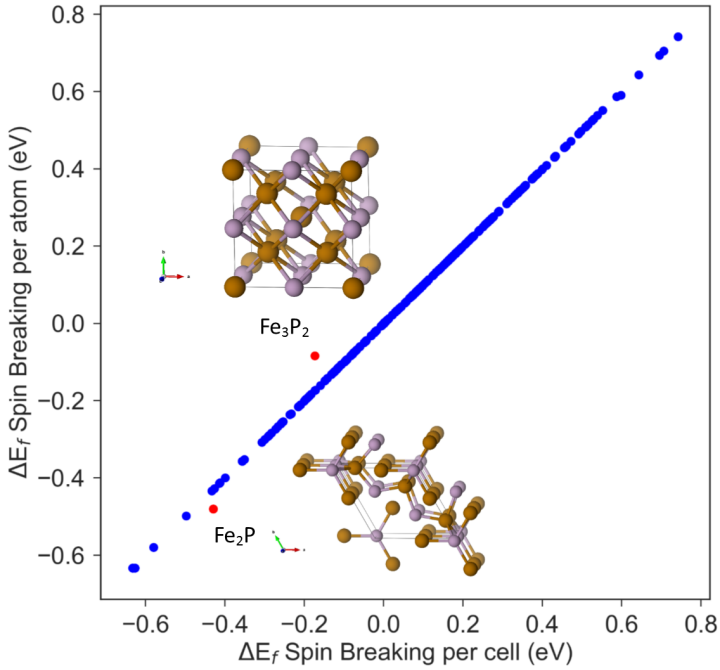

Fig. 4.2 Comparison between the formation energy of a spin symmetry broken in the cell versus on an atom by atom basis. The two structures with energy differences greater than 0.05, Fe_2P and Fe_3P_2 are visualised here with orange atoms as Fe and purple as P.

The difference in formation energy between breaking the spin symmetry across the cell compared to on each individual atom was more than 50 meV/atom for Fe_2P and Fe_3P_2 however neither structure was on the convex hull tie line after a full AIRSS search. Breaking the spin in the cell resulted in a non-magnetic (NM) Fe_2P and ferromagnetic (FM) Fe_3P_2 structure breaking the spin symmetry over the cell, and a FM Fe_2P and an anti-ferromagnetic (AFM) Fe_3P_2 structure breaking the spin by atom. The AFM Fe_3P_2 structure is destabilised by 80 meV/atom relative to the FM state, but given that AFM Fe_3P_2 has an energy over 350 meV/atom above the hull, this suggests the structure is unlikely to form in experiment. However, FM Fe_2P is stabilised by 50 meV/atom compared to FM Fe_2P, implying the higher spin state greatly stabilises this structure. Figure 4.3 shows the band structures and density of states for both NM (Figure 4.3a) and FM (Figure 4.3b) Fe_2P in which the FM ordering of the spins in FM Fe_2P is clear from the two patterns of spin symmetries for up and down spin channels. While neither FM nor NM Fe_2P was on the convex hull, it highlights the need to break the spin symmetry on an atom when re-optimising structures in order to find the ground-state spin orientations. However, given that these two structures are only 1% of all those surveyed, this suggests that initial high throughput calculations can be done with spin symmetry breaking in the unit cell,

using spin symmetry breaking atom-by-atom as a *post-hoc* step, in order to determine the true ground-state spin ordering of the bulk material. The following convex hulls are thus shown for atoms with spin symmetry broken only in the unit-cell.

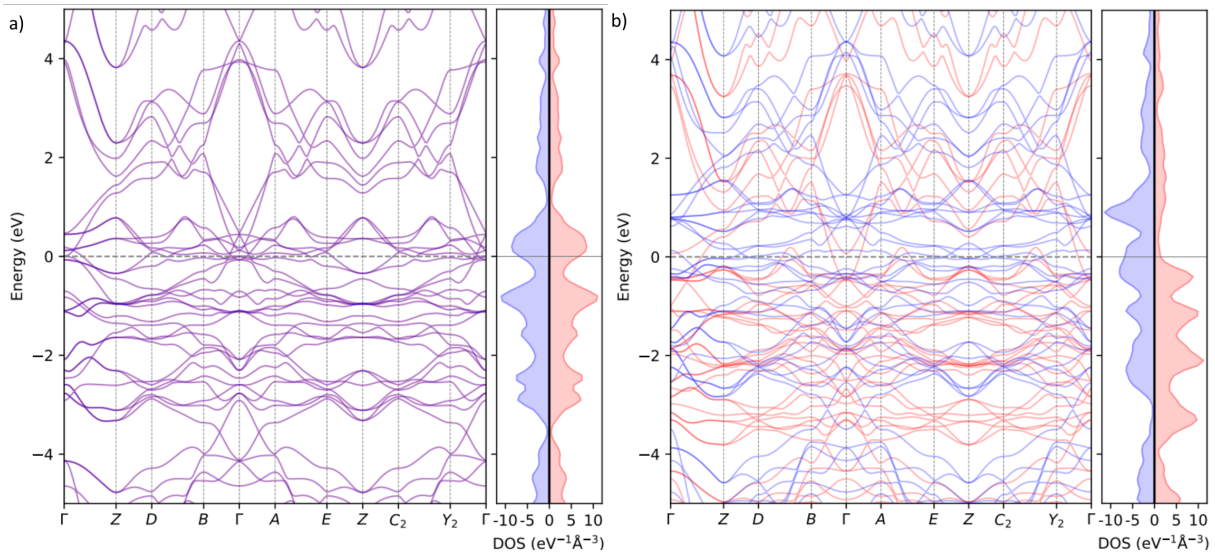

Fig. 4.3 a) Fe_2P band structure and density of states (DOS) with spin breaking across the cell, resulting in no spin-polarisation effects. Spin up channels are shown in red, with spin down in blue, making the overlap of these two channels purple, as shown in this band structure. The DOS plot is lined up with the band structure energies in the left tile. b) Band structure and DOS for Fe_2P with spin breaking on the first Fe atom, resulting in a spin polarised band structure, in which the DOS indicates this material is ferromagnetic, and the bands are now split by spin channel (up or down).

4.2 Fe-P AIRSS search

A search of 1200 Fe-P structures was carried out using both AIRSS, and structural prototypes from the OQMD database with Fe and P. The convex hull constructed from this search is shown in Figure 4.4. While no new stoichiometries of Fe-P were identified, several new phases of previously identified stoichiometries were found, shown in Figure 4.5 with details in Table 4.2. Fe_2P was swapped from Co_2P and FeP from AsFe. The new FeP structure was 6 meV/atom lower in energy than the ICSD structure, and the swap-identified Fe_2P structure was 68 meV/atom lower in energy than the ICSD structure. After breaking the spin symmetry on both phases of Fe_2P, the swap identified phase is still 19 meV/atom lower in energy than the ICSD structure, and both are ferromagnetic ordered structures. Although Fe_3P was on the convex hull before identifying the new phase of Fe_2P, following the AIRSS search, this raised the formation energy of Fe_3P to over 50 meV/atom above the convex hull tie-line.

Although many of these Fe-based compounds are magnetic, the ground-state structures of the P-rich structures (FeP_4 and FeP_2) have no spin character after geometry optimisation. This

is significant, given that these two compounds are the most viable for battery applications, given their high phosphorus content. In such a conversion anode, the majority of the capacity in these batteries will come from the contribution of phosphorus which will be converted, during discharge, to Na_3P. Thus, while Fe is present in these materials, it is likely that its magnetic nature will not affect the overall performance of the batteries for P-rich anodes that will give the highest capacity.

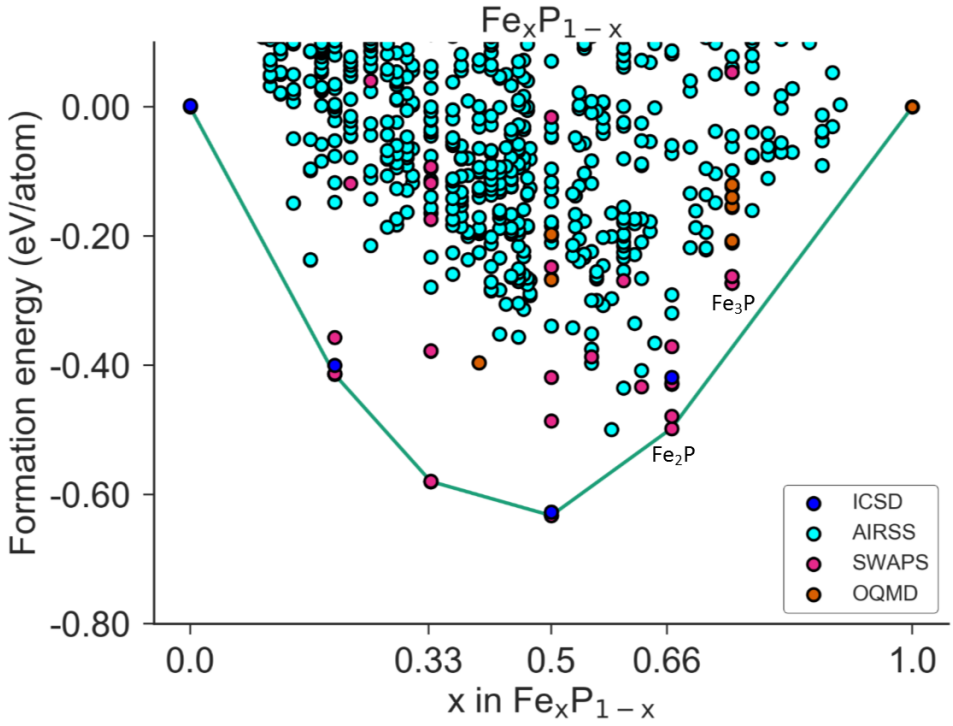

Fig. 4.4 A binary hull of Fe-P at 450 eV, 0.05 2π $Å^{-1}$ k-point spacing using the CASTEP QC5 set of pseudopotentials. Points in this figure are coloured by the method used to identify the structure, with SWAPS defined as those transition-metal pnictides from the OQMD whose atoms have been substituted ("swapped") for Fe and P.

4.3 Na-Fe-P ternary AIRSS search

Although the Li-Fe-P ternary system has two known ternary compounds, the Na-Fe-P ternary space has no known phases, and therefore an initial AIRSS search of 3000 structures was performed, the results are plotted in Figure 4.6. While this search would be more comprehensive by generating another few thousand structures, the initial results identify several structures negative in formation energy ($NaFe_2P_2$ and $Na_2Fe_{12}P_7$) and one structure NaFeP on the ternary hull, all shown in figure 4.5. Both $NaFe_2P_2$ and $Na_2Fe_{12}P_7$ were identified by swapping elements of known structures in the OQMD [9]. $NaFe_2P_2$ was swapped from $LiCu_2P_2$, further confirming the similarities between these two families of structures. $Na_2Fe_{12}P_7$ was swapped

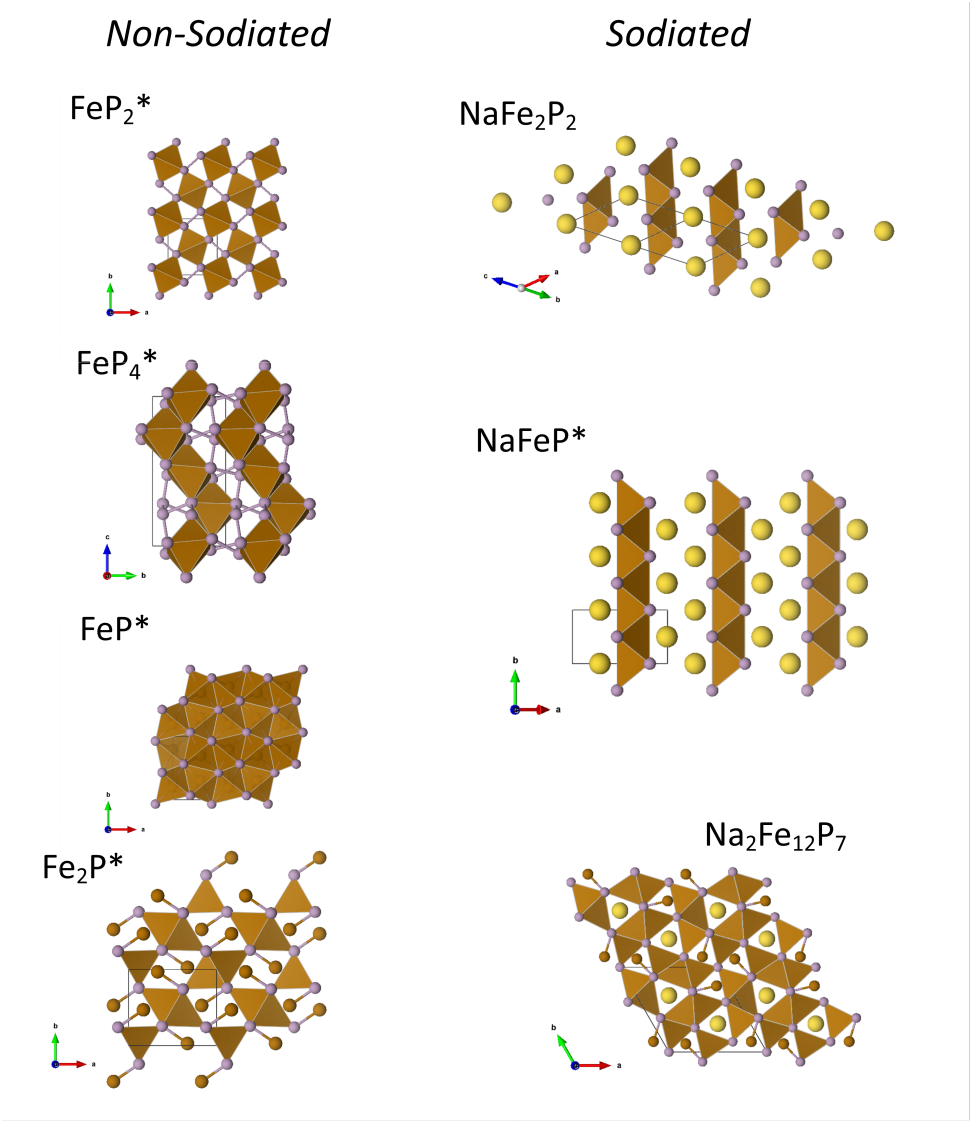

Fig. 4.5 The lowest energy configuration of each stoichiometry within 30 meV of the ternary hull tie line for Na-Fe-P divided into the sodiated and non-sodiated structures for visual comparison. The cutoff of 30 meV was chosen to sample the range of structures close to the hull, which could be stable at higher temperatures. Here, Na is in yellow, Fe in orange, and P in purple. The starred (*) structures are on the Na-Fe-P hull. Polyhedra around Fe atoms show the structural relationships between NaFeP and $NaFe_2P_2$, which have layers of iron phosphide chains separated by two or one layer of Na atoms respectively. $Na_2Fe_{12}P_7$ also is similar to Fe_2P with two Na atoms inserted for two Fe atoms from $Fe_{14}P_7$

from $Li_2Ni_{12}P_7$. In this hull, the Na-Fe edge has no structures, as experimental studies show Na does not alloy with Fe. While an AIRSS search for these structures could be performed in the future, one was not carried out for the purposes of this analysis.

Material	Space Group	No. f.u.	Vol/f.u. (Å^3)	Hull dist. (meV/atom)	Provenance
FeNaP *	*Pm*	2	48.60	0.00	AIRSS
Fe_2NaP_2	*I4/mmm*	1	69.93	14.82	SWAPS
$Fe_{12}Na_2P_7$	*Pm*	1	250.21	27.26	SWAPS
Fe_2P *	*Pnma*	4	32.73	0.00	SWAPS
Fe_2P	*Pm*	3	32.2	0.205	ICSD
FeP *	*Pnma*	4	22.70	0.00	SWAPS
FeP	*P*	4	22.64	5.69	ICSD
FeP_2 *	*Pnnm*	2	38.17	0.00	ICSD
Fe_1P_4 *	*P1*	4	73.35	0.00	ICSD

Table 4.2 Structures within 50 meV/atom of the ternary Na-Fe-P hull, with those structures which are predicted to be stable at 0K, thus are at the vertex of a convex hull tie line are denoted by an asterisk (*). Here f.u. is formula-unit.

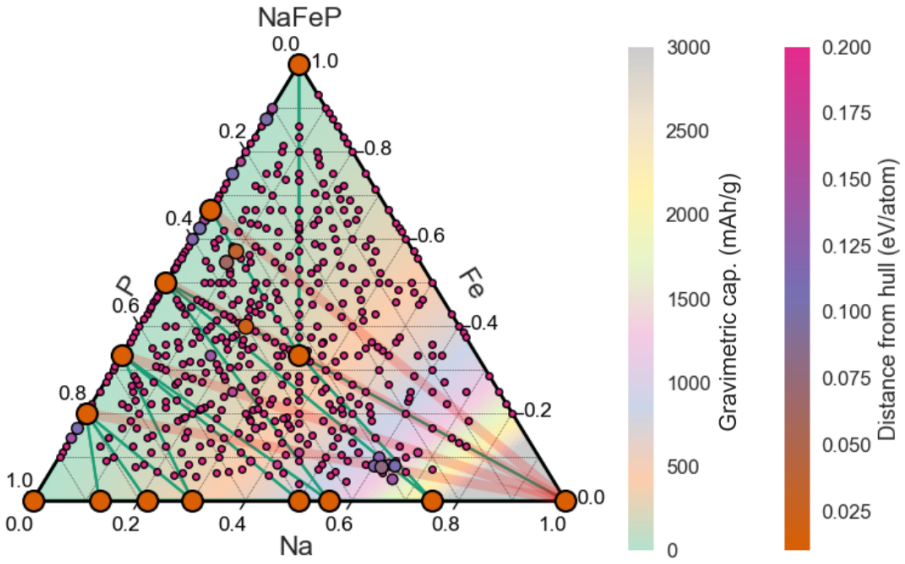

Fig. 4.6 Ternary hull between Na, Fe, and P. There are no structures on the hull tie line between Na and Fe as no binaries of these compounds exist. The Na-P structures are taken from [25]. The hull is shaded by gravimetric capacity of each structure, and red lines connect binary Fe-P structures to Na. The points are individual structures and are coloured by their distance from the hull, with larger points being lower information energy and large orange points connected by green tie lines being on the hull. NaFeP is at the centre of the hull, shown with an orange point.

4.4 Na-Fe-P ternary voltage profile

From the formation energies in Figure 4.6, ternary voltage curves were constructed between the Fe-P binary structures and Na, shown in Figure 4.7b. Of the four structures on the binary

Fe-P hull, only FeP_4 and FeP_2 show voltage differences between the binary structures and Na, suggesting that only these two structures could be sodiated as an anode in Na^+ ion batteries; in Figure 4.7b, both FeP and Fe_2P have flat, two-phase voltage profiles, suggesting that they would not be able to cycle in a battery, given that a potential difference is required to allow ions to flow through the battery during cycling. Further experiments by Zhang *et al.* showed that in fact FeP_2 also had a flat two-phase voltage profile when cycled versus lithium, and from the orange voltage curve in Figure 4.7a, we can see that there is only a 0.1V difference between FeP_2 starting products at 0.3 V and end products at 0.2 V, which could be the cause for Zhang and coworkers being unable to cycle FeP_2 [21]. On the other hand FeP_4 shows excellent agreement with their experimental results, shown in Figure 4.7b, in which they cycled FeP_4 from 1.0V to 0.25V, with an initial capacity of 1417 mAh/g, which stabilised at around 1100 mAh/g for the first 30 cycles. This initial capacity is almost at the theoretical limit presented here of 1491 mAh/g for FeP_4, suggesting that the NaFeP structure may play a role in the experimental voltage curve by contributing both to capacity and stability.

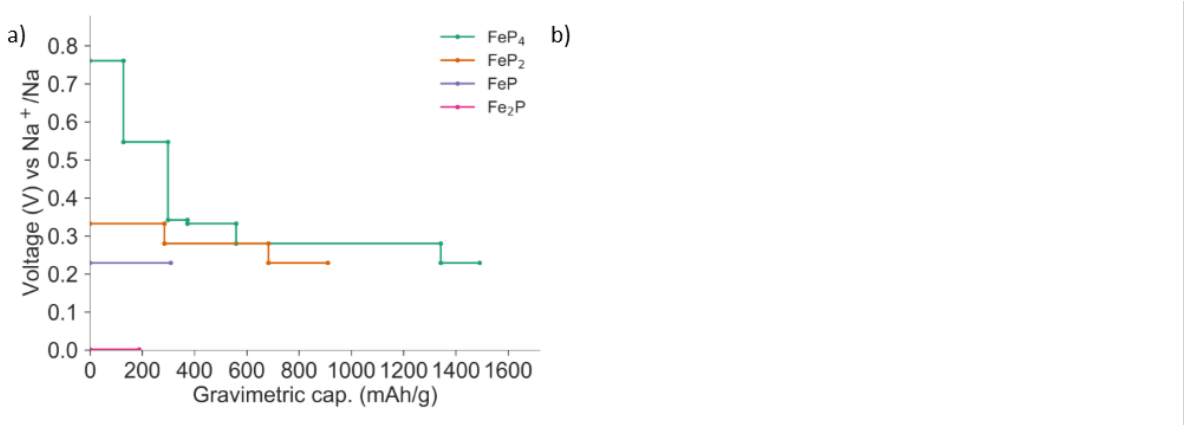

Fig. 4.7 a) Theoretical voltage curve corresponding to the four starting structures in the Fe-P binary phase diagram. b) Experimental voltage curves adapted from [21] for FeP_4 Na^+ ion battery. Reused with permission, ©2016 Elsevier B.V. In redacted version please refer to ref. [21] Figure 3b for image. The details of each step for the FeP_4 reaction (green) are shown in Appendix A. The 1^{st} and 2^{nd} cycles of the FeP_4 experimental battery are shown in black and red respectively, and match well with the corresponding capacities in the theoretical voltage curve from this work shown in green in a.

While FeP_4 has been tested as an anode for both Li^+ and Na^+ ion batteries, the full chemical reaction between FeP_4 and Na or Li has yet to be characterised fully. In the Li-FeP_4 case, the FeP_4 anode showed poor cycling stability, attributed to an unknown mechanism preventing the formation of the LiFeP ternary structure which stabilised the other Li-ion anode reactions [82]. However, in this case of Na-FeP_4, it is likely that a ternary stabilising structure, NaFeP, is formed during cycling because both experimental studies and this theoretical study show that the FeP_4 anode is the most likely candidate for cycling in a Na^+ ion battery [21]. The proposed steps of the voltage curve cycling are given in Appendix A, and suggest that FeNaP forms

at around 0.23V. The experimental voltage profile in Figure 4.7b, has an extended plateau at 0.25V which Zhang attributes to the conversion reaction between FeP_4 and Na during the first cycle, but in the second cycles and beyond, the plateau exists at 0.3 V, suggesting a different mechanism is occurring [21]. The plateau at 0.25V is consistent in the theoretical reaction with the formation of the ternary structure NaFeP, and at 0.3 V with the formation of either Na_5P_4 + FeP at 0.33 V or FeP + Na_3P at 0.28 V. These initial results thus suggest that while FeP_4 was thought to undergo a conversion reaction with Na^+ on discharge, in reality, there is an insertion mechanism combined with the formation of NaFeP, which could explain the increased cyclability seen experimentally for this structure.

4.5 Conclusions

Performing crystal structure prediction on a system containing magnetic elements such as iron adds a degree of freedom to the calculations which greatly increases the computational time needed for searching. However, this study showed that initial searches could be carried out without breaking the spin symmetry on each atom in a cell, and only afterwards identifying the ground state magnetic ordering using a full spin symmetry breaking geometry optimisation to understand the electronic structure of the ground-state. Despite this added level of complexity it was still possible to carry out a preliminary AIRSS search on both Fe-P and Na-Fe-P, which identified a new ternary NaFeP structure, and a new magnetic phase of Fe_2P. Furthermore, constructing a ternary voltage curve which contained this new NaFeP structure suggests that structure could form upon sodiation, given the good comparison between the computational and experimental voltage curves for this system. A chemical reaction was proposed for FeP_4, which had not yet been characterised due to the complex nature, of what I have suggested is likely an insertion mechanism. The new NaFeP phase implies that iron phosphides would be insertion anodes rather than conversion anodes as previously suggested. While this phase is likely stabilising during cycling, the total theoretical capacity of FeP_4 is lowered by 298 mAh/g with the addition of NaFeP (from 1789 mAh/g to 1491 mAh/g). Although the NaFeP phase may hinder FeP_4 battery capacity, it provides a better understanding of the FeP_4 voltage profile and insertion mechanism. While a complete understanding of the sodium iron phosphides requires a full AIRSS search for all magnetic and structural ground-states, these findings are a promising comparison to published experimental results.

Chapter 5

Conclusions and outlook

5.1 Conclusions

At the outset, this study of two related transition-metal phosphide systems was an attempt to identify novel structures for Li and Na-ion batteries which could improve the performance of future battery technologies. However, upon conducting several AIRSS searches on Cu-P, Cu-Li, Fe-P, and Na-Fe-P, many interesting phenomena of these systems urged a deeper look into the electronic and kinetic properties of the copper phosphides as well as the magnetic properties of the iron phosphides.

An experimentally elusive compound Cu_2P was identified within the copper phosphide system, which had a bulk structure analogous to both Rh_2P and Ir_2P, and an electronic structure which suggests this material could be a new semimetal, if it could be synthesised. Further analysis of the Cu_3P structure, known to have several Cu vacancies, suggested that the ground-state stoichiometry is Cu_8P_3, although this structure still had a ground-state enthalpy above the Cu-P convex hull. A finite temperature hull of this system showed that adding in entropy did lower Cu_8P_3 in energy, but that there were still unknown contributions preventing it from being on the hull at finite temperature. A high-pressure study of Cu-P at both 10GPa and 100GPa suggests that there are several Cu rich structures at high pressures which have not yet been studied, but are predicted by these computational results.

Within the Cu-Li system, a novel CuLi compound was identified by AIRSS, though the literature suggests that temperature dependence plays a large role in this system, as the existence of many of the Cu-Li compounds, especially Cu_4Li and Cu_2Li_3 have been questioned in the literature. However, this analysis of the CuLi system also had implications for battery materials. The CuLi compound on the ternary Li-Cu-P hull suggests that some Cu-Li compounds do form upon cycling of a CuP_2 battery because the experimental initial capacity was higher than the theoretical capacity for CuP_2 not considering Cu-Li compounds, but lower than the capacity when taking them into consideration. Furthermore, constructing the voltage profile for an already synthesised CuP_{10} compound suggests that this may be a better alternative for higher

capacity transition metal phosphide anodes, given its high theoretical capacity. It is likely that this material has just been overlooked in experimental studies, and should be investigated in the future.

In an effort to study a lower-cost transition-metal phosphide system, a crystal structure search was also conducted on both Fe-P and Na-Fe-P. In this case, the ferromagnetic nature of Fe played a large role in these AIRSS searches, and greatly increased the computational complexity of the geometry optimisation and the overall size of the potential energy surface being searched. While a full AIRSS search was not conducted, initial results have still identified one structure, NaFeP, with a negative formation energy which is on the ternary convex hull. The ternary voltage profile for this system closely match with experimental results for FeP_4 anodes, and suggested that further experiments be conducted in order to determine the exact nature of the Na-FeP_4 insertion process. From this study, I have determined that this process likely includes a ternary stabilising structure during cycling, which may also lower the capacity of the anode.

5.2 Outlook

Any computational study on something as relevant as Li-ion batteries would be remiss without an accompanying experimental counterpart. Therefore, the next steps of this study would be to synthesise the Cu-P and Fe-P compounds mentioned above and cycle them in a half-cell with Li and Na respectively. In this case, NMR and XRD spectral can be especially useful for direct comparison with the compounds identified by AIRSS, and the temperature dependent voltage profiles can serve as a method of bringing these DFT studies towards experimental comparison.

Additionally, an attempt to crystallise Cu_2P could provide answers as to why this compound does not form, or perhaps identify a new route for forming this novel semimetal material. By synthesising NaFeP or identifying it during the cycling of a Na-ion battery cell, it would be possible to confirm the conversion mechanism of FeP_4. Additionally, once the AIRSS searches of this ternary Na-Fe-P space have been completed, it will be necessary to identify not only the geometric ground-state structures, but also the magnetic orientations of the spins in these structures, and possibly consider spin-orbit coupling or different functionals which may change the character of these convex hulls. A more in-depth study of this ternary system may also identify other ternary compounds, and new metallic phases.

Overall, this work has provided an initial study in several transition-metal phosphide groups, which have relevance not only in the battery community but also within solid state physics. I have addressed ways to incorporate spin states into high throughput computational searches within the context of iron phosphide anodes, which could be easily applied to other systems of magnetic materials. The temperature dependent calculations on copper phosphides are also

widely transferable to any system, and can be used to create a temperature dependent voltage profile as well. This dissertation has suggested several future pathways for both computational and experimental work to investigate, in order to further understand these transition metal phosphide systems, and provided meaningful insights into two battery anode materials.

Chapter 6

Appendix A

Li-Cu-P voltage profile reactions

The following tables give detailed reactions for each voltage profile in Figure 3.7 and. Each voltage profile corresponds to one of the red pathways shown in Figure 3.6 and again here in more detail in Figure 6.1. The reactions are determined by following a red pathway in Figure 6.1 from the binary Cu-P phase to Li, with a new reaction occurring each time the red pathway crosses a green tie-line on the ternary hull. This corresponds to a region between two points on the green tie line, and thus a horizontal two-phase portion of the voltage profile shown in Figure 3.7. Voltages and gravimetric capacities are for each reaction step. The reactions are given assuming the CuLi and Cu_2Li phases form, and a dashed line is shown between the reactions which do not include Cu-Li phases, and those which do (similar to the dashed line shown in Figure 3.7 on the voltage profile). The fraction of Li added is the relative amount of Li added in each step (each row of the table) over a full reaction pathway which would add one Li atom in total.

CuP_{10} + 31 Li ⟶ CuLi + $10Li_3P$			
Gravimetric Capacity (mAh/g)	Voltage (V)	Reaction	Fraction of Li added
67	1.22	CuP_{10} + xLi ⟶ LiP_7 + Cu_2P_7	0.08
200	1.19	LiP_7 + Cu_2P_7 + xLi ⟶ Li_3P_7 + Cu_2P_7	0.12
351	1.04	Li_3P_7 + Cu_2P_7 + xLi ⟶ Li_3P_7 + $Cu_4Li_5P_6$	0.11
700	0.89	Li_3P_7 + $Cu_4Li_5P_6$ + xLi ⟶ LiP + $Cu_4Li_5P_6$	0.16
2082	0.86	LiP + $Cu_4Li_5P_6$ + xLi ⟶ LiP + $CuLi_2P$	0.03
2153	0.84	LiP + $CuLi_2P$ + xLi ⟶ $CuLi_2P$ + Li_3P	0.23
2190	0.52	$CuLi_2P$ + Li_3P + xLi ⟶ Li_3P + Cu	0.01
2226	0.10	Li_3P + Cu + xLi ⟶ Cu_2Li + Li_3P	0.003
2226	0.06	Cu_2Li + Li_3P + xLi ⟶ CuLi + Li_3P	0.003

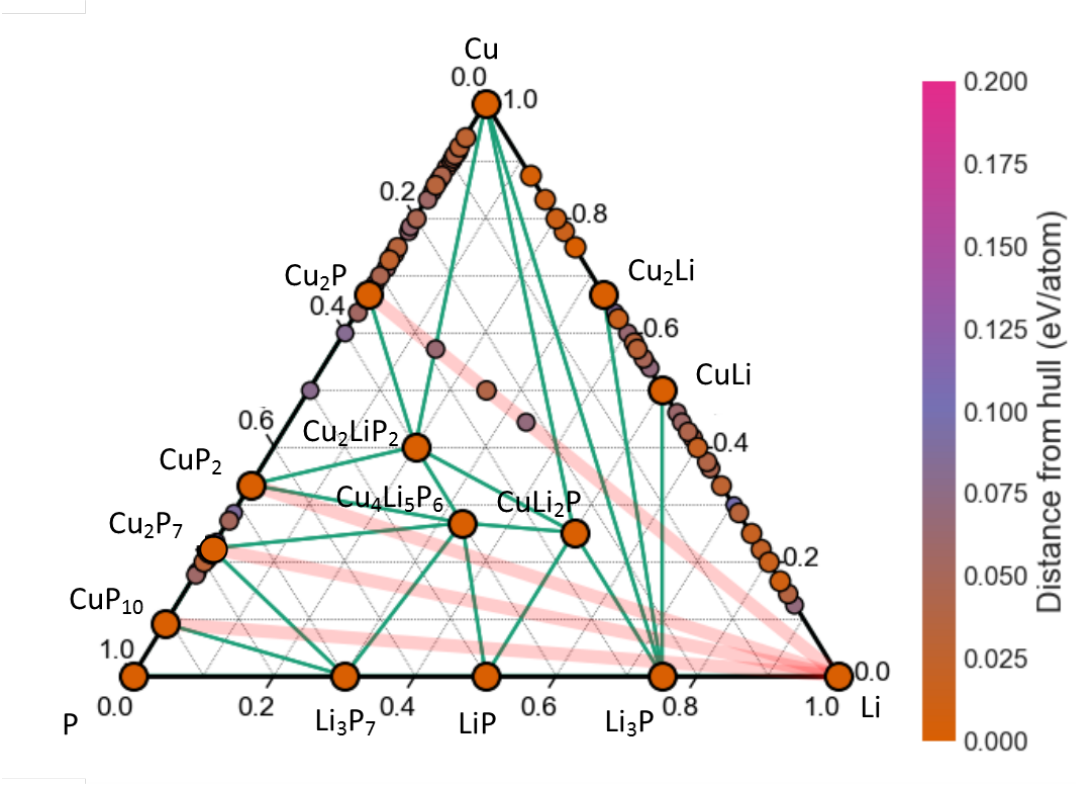

Fig. 6.1 Ternary hull between Li-Cu-P with points coloured and sized by hull distance with larger points closer to the hull, pathways from binary Cu-P structures to Li coloured in red. Structures on the hull are shown as large orange points, and labelled with their corresponding structures. Green tie lines connect the hull structures, and correspond to changes from one reaction to the next along a red pathway.

$Cu_2P_7 + 23Li \longrightarrow 2CuLi + 7Li_3P$			
Gravimetric Capacity (mAh/g)	Voltage (V)	Reaction	Fraction of Li added
328	1.04	$Cu_2P_7 + xLi \longrightarrow Li_3P_7 + Cu_4Li_5P_6$	0.31
507	0.89	$Li_3P_7 + Cu_4Li_5P_6 + xLi \longrightarrow LiP + Cu_4Li_5P_6$	0.10
1481	0.86	$LiP + Cu_4Li_5P_6 + xLi \longrightarrow LiP + CuLi_2P$	0.08
1637	0.84	$LiP + CuLi_2P + xLi \longrightarrow Li_3P + CuLi_2P$	0.18
1715	0.52	$Li_3P + CuLi_2P + xLi \longrightarrow Li_3P + Cu$	0.02
1796	0.10	$Li_3P + Cu + xLi \longrightarrow Li_3P + Cu_2Li$	0.01
1796	0.06	$Li_3P + Cu_2Li + xLi \longrightarrow CuLi + Li_3P$	0.01

$CuP_2 + 7Li \longrightarrow CuLi + 2Li_3P$			
Gravimetric Capacity (mAh/g)	Voltage (V)	Reaction	Fraction of Li added
200	1.07	$CuP_2 + xLi \longrightarrow Cu_2P_7 + Cu_4Li_5P_6$	0.23
313	1.04	$Cu_2P_7 + Cu_4Li_5P_6 + xLi \longrightarrow Li_3P_7 + Cu_4Li_5P_6$	0.09
374	0.89	$Li_3P_7 + Cu_4Li_5P_6 + xLi \longrightarrow LiP + Cu_4Li_5P_6$	0.04
1068	0.86	$LiP + Cu_4Li_5P_6 + xLi \longrightarrow LiP + CuLi_2P$	0.13
1282	0.84	$LiP + CuLi_2P + xLi \longrightarrow Li_3P + CuLi_2P$	0.13
1388	0.52	$Li_3P + CuLi_2P + xLi \longrightarrow Cu + Li_3P$	0.04
1495	0.10	$Cu + Li_3P + xLi \longrightarrow Cu_2Li + Li_3P$	0.02
1495	0.06	$Cu_2Li + Li_3P + xLi \longrightarrow CuLi + Li_3P$	0.02

$Cu_2P + 5Li \longrightarrow 2CuLi + Li_3P$			
Gravimetric Capacity (mAh/g)	Voltage (V)	Reaction	Fraction of Li added
85	1.19	$Cu_2P + xLi \longrightarrow Cu_2LiP2 + Cu$	0.14
339	0.94	$CuLi_2P + Cu + xLi \longrightarrow Cu_2LiP2 + Cu$	0.26
509	0.52	$Cu_2LiP2 + Cu + xLi \longrightarrow Li_3P + Cu$	0.1
678	0.10	$Cu + Li_3P + xLi \longrightarrow Cu_2Li + Li_3P$	0.07
848	0.06	$Cu_2Li + Li_3P + xLi \longrightarrow CuLi + Li_3P$	0.05

Na-Fe-P voltage profile reactions

As in the above section, the following tables detail reactions for the voltage profiles shown in Figure 4.7a. Each voltage profile corresponds to one of the red pathways shown in Figure 4.6. Each reaction corresponds to a horizontal two-phase portion of the voltage profile, and values here are given for the voltage that each reaction occurs at, as well as the gravimetric capacity calculated for each reaction step. In this ternary diagram, shown in Figure 6.2 two phases (Fe_2P and FeP) have only a single reaction from Fe-P to Na, and thus have a horizontal line as a voltage profile in Figure 4.7, and only cross one green tie line on the hull in Figure 6.2. The fraction of Na added is the relative amount of Na being added in each step (each row of the table) over a full reaction pathway (which would add one Na atom in total). At the top of each table the balanced full reaction is given.

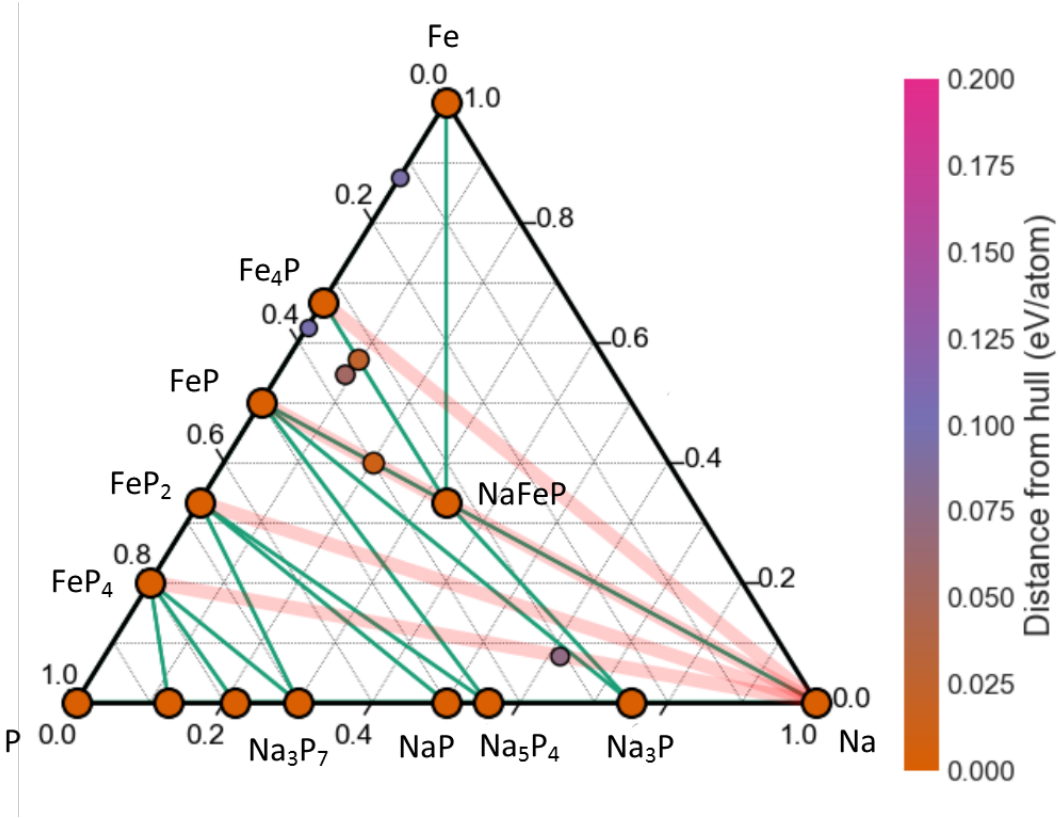

Fig. 6.2 Ternary hull between Na-Fe-P with points coloured and sized by hull distance with larger points closer to the hull, pathways from binary Fe-P structures to Na coloured in red. Structures on the hull are shown as large orange points, and labelled with their corresponding structures. Green tie lines connect the hull structures, and correspond to changes from one reaction to the next along a red pathway.

$FeP_4 + 10Na \longrightarrow Na_3P + NaFeP$			
Gravimetric Capacity (mAh/g)	Voltage (V)	Reaction	Fraction of Li added
128	0.76	$FeP_4 + xNa \longrightarrow Na_3P_7 + FeP_2$	0.14
298	0.54	$FeP_2 + Na_3P_7 + xNa \longrightarrow NaP + FeP_2$	0.14
373	0.34	$FeP_2 + NaP + xNa \longrightarrow Na_5P_4 + FeP_2$	0.05
559	0.33	$FeP_2 + Na_5P_4 + xNa \longrightarrow Na_5P_4 + FeP$	0.09
1342	0.28	$FeP + Na_5P_4 + xNa \longrightarrow FeP + Na_3P$	0.21
1491	0.23	$FeP + Na_3P + xNa \longrightarrow Na_3P + NaFeP$	0.02

$FeP_2 + 4Na \longrightarrow Na_3P + NaFeP$			
Gravimetric Capacity (mAh/g)	Voltage (V)	Reaction	Fraction of Li added
284	0.33	$FeP_2 + xNa \longrightarrow Na_5P_4 + FeP$	0.29
683	0.28	$FeP + Na_5P_4 + xNa \longrightarrow Na_3P + FeP$	0.21
910	0.23	$FeP + Na_3P + xNa \longrightarrow Na_3P + NaFeP$	0.07

$FeP + Na \longrightarrow 0Na_3P + NaFeP$			
Gravimetric Capacity (mAh/g)	Voltage (V)	Reaction	Fraction of Li added
309	0.23	$FeP + xNa \longrightarrow Na_3P + NaFeP$	0.33

$Fe_2P + Na \longrightarrow Fe + NaFeP$			
Gravimetric Capacity (mAh/g)	Voltage (V)	Reaction	Fraction of Na added
189	0.0	$Fe_2P + xNa \longrightarrow Fe + NaFeP$	0.25

References

[1] C. A. Horowitz, "Paris agreement," *International Legal Materials*, vol. 55, no. 4, pp. 740–755, 2016.

[2] M. den Elzen, N. Höhne, K. Jiang, J. Cantzler, P. Drost, T. Fransen, H. Fekete, T. Kuramochi, D. Lee, and K. Levin, "Methodology of national and global studies-the emissions gap report 2017 chapter 3 appendix a," *The Emissions Gap Report 2017: A UN Environment Synthesis Report*, 2017.

[3] K. Mizushima, P. Jones, P. Wiseman, and J. Goodenough, "Li_xCoO_2 (0<x<-1): A new cathode material for batteries of high energy density," *Materials Research Bulletin*, vol. 15, no. 6, pp. 783 – 789, 1980.

[4] Y. Mekonnen, A. Sundararajan, and A. I. Sarwat, "A review of cathode and anode materials for lithium-ion batteries," *SoutheastCon 2016*, pp. 1–6, 2016.

[5] C. Vaalma, D. Buchholz, M. Weil, and S. Passerini, "A cost and resource analysis of sodium-ion batteries," *Nat. Rev. Mater.*, vol. 3, no. 4, p. 18013, 2018.

[6] N. Nitta, F. Wu, J. T. Lee, and G. Yushin, "Li-ion battery materials: present and future," *Biochemical Pharmacology*, vol. 18, no. 5, pp. 252–264, 2015.

[7] S. Kirklin, B. Meredig, and C. Wolverton, "High-throughput computational screening of new Li-ion battery anode materials," *Advanced Energy Materials*, vol. 3, no. 2, pp. 252–262, 2013.

[8] N. Yabuuchi, K. Kubota, M. Dahbi, and S. Komaba, "Research development on sodium-ion batteries.," *Chem. Rev.*, vol. 114, no. 23, pp. 11636–11682, 2014.

[9] S. Kirklin, J. E. Saal, B. Meredig, A. Thompson, J. W. Doak, M. Aykol, S. Rühl, and C. Wolverton, "The Open Quantum Materials Database (OQMD): assessing the accuracy of DFT formation energies," *npj Comp. Mater.*, vol. 1, no. 1, p. 15010, 2015.

[10] W. Li, Z. Yang, M. Li, Y. Jiang, X. Wei, X. Zhong, L. Gu, and Y. Yu, "Amorphous red phosphorus embedded in highly ordered mesoporous carbon with superior lithium and sodium storage capacity," *Nano Letters*, vol. 16, no. 3, pp. 1546–1553, 2016.

[11] Y. Fuhua, G. Hong, C. Jun, and G. Zaiping, "Phosphorus-based materials as the anode for sodium-ion batteries," *Small Methods*, vol. 1, no. 11, p. 1700216, 2017.

[12] B. Mauvernay, M. P. Bichat, F. Favier, L. Monconduit, M. Morcrette, and M. L. Doublet, "Progress in the lithium insertion mechanism in Cu_3P," *Ionics*, vol. 11, no. 1-2, pp. 36–45, 2005.

[13] S. Boyanov, D. Zitoun, M. Ménétrier, J. C. Jumas, M. Womes, and L. Monconduit, "Comparison of the electrochemical lithiation/delithiation mechanisms of FeP_x (x = 1, 2, 4) based electrodes in Li-ion batteries," *J. Phys. Chem. C*, vol. 113, no. 51, pp. 21441–21452, 2009.

[14] F. Poli, A. Wong, J. S. Kshetrimayum, L. Monconduit, and M. Letellier, "In Situ NMR Insights into the Electrochemical Reaction of Cu_3P Electrodes in Lithium Batteries," *Chem. Mater.*, vol. 28, no. 6, pp. 1787–1793, 2016.

[15] H. Pfeiffer, F. Tancret, M. P. Bichat, L. Monconduit, F. Favier, and T. Brousse, "Air stable copper phosphide (Cu_3P: A possible negative electrode material for lithium batteries," *Electrochemistry Communications*, vol. 6, no. 3, pp. 263–267, 2004.

[16] M.-P. Bichat, T. Politova, H. Pfeiffer, F. Tancret, L. Monconduit, J.-L. Pascal, T. Brousse, and F. Favier, "Cu_3P as anode material for lithium ion battery: powder morphology and electrochemical performances," *Journal of Power Sources*, vol. 136, pp. 80–87, 2004.

[17] K. Wang, J. Yang, J. Xie, B. Wang, and Z. Wen, "Electrochemical reactions of lithium with CuP_2 and $Li_{1.75}Cu_{1.25}P_2$ synthesized by ballmilling," *Electrochemistry Communications*, vol. 5, no. 6, pp. 480 – 483, 2003.

[18] S.-O. Kim and A. Manthiram, "Phosphorus-rich CuP_2 embedded in carbon matrix as a high-performance anode for lithium-ion batteries," *ACS applied materials & interfaces*, vol. 9, no. 19, pp. 16221–16227, 2017.

[19] S. Liu, X. He, J. Zhu, L. Xu, and J. Tong, "Cu_3P/RGO nanocomposite as a new anode for lithium-ion batteries," *Scientific reports*, vol. 6, p. 35189, 2016.

[20] S. Lange, M. Bawohl, R. Weihrich, and T. Nilges, "Mineralization routes to polyphosphides: Cu_2P_{20} and Cu_5InP_{16}," *Angewandte Chemie - International Edition*, vol. 47, no. 30, pp. 5654–5657, 2008.

[21] W. Zhang, M. Dahbi, S. Amagasa, Y. Yamada, and S. Komaba, "Iron phosphide as negative electrode material for Na-ion batteries," *Electrochemistry Communications*, vol. 69, pp. 11–14, 2016.

[22] A. Jain, S. P. Ong, G. Hautier, W. Chen, W. D. Richards, S. Dacek, S. Cholia, D. Gunter, D. Skinner, G. Ceder, and K. A. Persson, "Commentary: The Materials Project: A materials genome approach to accelerating materials innovation," *APL Materials*, vol. 1, no. 1, p. 011002, 2013.

[23] M. J. Mehl, D. Hicks, C. Toher, O. Levy, R. M. Hanson, G. Hart, and S. Curtarolo, "The aflow library of crystallographic prototypes: Part 1," *Comp. Mater. Sci.*, vol. 136, pp. S1 – S828, 2017.

[24] G. Bergerhoff, I. Brown, F. Allen, *et al.*, "Crystallographic databases," *International Union of Crystallography, Chester*, vol. 360, pp. 77–95, 1987.

[25] M. Mayo, K. J. Griffith, C. J. Pickard, and A. J. Morris, "Ab initio study of phosphorus anodes for Lithium- and Sodium-ion batteries," *Chem. Mater.*, vol. 28, no. 7, pp. 2011–2021, 2016.

[26] A. J. Morris, C. Grey, and C. J. Pickard, "Thermodynamically stable lithium silicides and germanides from density functional theory calculations," *Physical Review B*, vol. 90, no. 5, p. 054111, 2014.

[27] C. J. Pickard and R. J. Needs, "High-pressure phases of silane," *Phys. Rev. Lett.*, vol. 97, p. 045504, 2006.

[28] C. J. Pickard and R. J. Needs, "Ab initio random structure searching," *J. Phys. Condens. Matter*, vol. 23, no. 23, pp. 53201–23, 2011.

[29] M. Born and R. Oppenheimer, "Zur quantentheorie der molekeln," *Annalen der Physik*, vol. 389, no. 20, pp. 457–484, 1927.

[30] D. R. Hartree, "The wave mechanics of an atom with a non-coulomb central field. part i. theory and methods," *Mathematical Proceedings of the Cambridge Philosophical Society*, vol. 24, no. 1, p. 89–110, 1928.

[31] V. Fock, "Näherungsmethode zur lösung des quantenmechanischen mehrkörperproblems," *Zeitschrift für Physik*, vol. 61, no. 1, pp. 126–148, 1930.

[32] J. C. Slater, "Note on hartree's method," *Phys. Rev.*, vol. 35, pp. 210–211, 1930.

[33] P. Hohenberg and W. Kohn, "Inhomogeneous electron gas," *Phys. Rev.*, vol. 136, pp. B864–B871, 1964.

[34] W. Kohn and L. J. Sham, "Self-consistent equations including exchange and correlation effects," *Phys. Rev.*, vol. 140, pp. A1133–A1138, 1965.

[35] J. P. Perdew and K. Schmidt, "Jacob's ladder of density functional approximations for the exchange-correlation energy," *AIP Conference Proceedings*, vol. 577, no. 1, pp. 1–20, 2001.

[36] J. P. Perdew, K. Burke, and M. Ernzerhof, "Generalized gradient approximation made simple," *Phys. Rev. Lett.*, vol. 77, pp. 3865–3868, 1996.

[37] F. Bloch, "Über die quantenmechanik der elektronen in kristallgittern," *Zeitschrift für Physik*, vol. 52, no. 7, pp. 555–600, 1929.

[38] M. C. Payne, M. P. Teter, D. C. Allan, T. A. Arias, and J. D. Joannopoulos, "Iterative minimization techniques for ab initio total-energy calculations: molecular dynamics and conjugate gradients," *Rev. Mod. Phys.*, vol. 64, pp. 1045–1097, 1992.

[39] H. J. Monkhorst and J. D. Pack, "Special points for brillouin-zone integrations," *Physical review B*, vol. 13, no. 12, p. 5188, 1976.

[40] D. R. Hamann, M. Schlüter, and C. Chiang, "Norm-conserving pseudopotentials," *Phys. Rev. Lett.*, vol. 43, pp. 1494–1497, 1979.

[41] D. Vanderbilt, "Soft self-consistent pseudopotentials in a generalized eigenvalue formalism," *Phys. Rev. B*, vol. 41, pp. 7892–7895, 1990.

[42] M. D. Segall, P. J. D. Lindan, M. J. Probert, C. J. Pickard, P. J. Hasnip, S. J. Clark, and M. C. Payne, "First-principles simulation: ideas, illustrations and the CASTEP code," *J. Phys. Cond. Mat.*, vol. 14, no. 11, p. 2717, 2002.

[43] S. Clark, M. Segall, C. Pickard, P. Hasnip, M. Probert, K. Refson, and M. Payne, "First principles methods using CASTEP," *Zeitschrift für Kristallographie*, vol. 220, no. 5-6, pp. 567–570, 2005.

[44] S. L. Cunningham, "Special points in the two-dimensional Brillouin zone," *Physical Review B*, vol. 10, no. 12, pp. 4988–4994, 1974.

[45] Y. Hinuma, G. Pizzi, Y. Kumagai, F. Oba, and I. Tanaka, "Band structure diagram paths based on crystallography," *Comp. Mater. Sci.*, vol. 128, pp. 140–184, 2017.

[46] M. T. Dove, *Introduction to Lattice Dynamics*. Cambridge Topics in Mineral Physics and Chemistry, Cambridge University Press, 1993.

[47] K. Momma and F. Izumi, "VESTA 3 for three-dimensional visualization of crystal volumetric and morphology data," *J. Appl. Crystallogr.*, vol. 44, pp. 1272–1276, 2011.

[48] R. Fletcher, "A new approach to variable metric algorithms," *The Computer Journal*, vol. 13, no. 3, pp. 317–322, 1970.

[49] B. G. Pfrommer, M. Côté, S. G. Louie, and M. L. Cohen, "Relaxation of crystals with the quasi-newton method," *Journal of Computational Physics*, vol. 131, no. 1, pp. 233–240, 1997.

[50] F. H. Stillinger and D. K. Stillinger, "Cluster optimization simplified by interaction modification," *J. Chem. Phys.*, vol. 93, no. 8, pp. 6106–6107, 1990.

[51] C. J. Pickard and R. J. Needs, "Aluminium at terapascal pressures," *Nat. Mater.*, vol. 9, no. 8, pp. 624–627, 2010.

[52] A. J. Morris, C. J. Pickard, and R. J. Needs, "Hydrogen/nitrogen/oxygen defect complexes in silicon from computational searches," *Phys. Rev. B*, vol. 80, p. 144112, 2009.

[53] A. J. Morris, R. J. Needs, E. Salager, C. P. Grey, and C. J. Pickard, "Lithiation of silicon via lithium zintl-defect complexes from first principles," *Phys. Rev. B*, vol. 87, p. 174108, 2013.

[54] J. M. Stratford, M. Mayo, P. K. Allan, O. Pecher, O. J. Borkiewicz, K. M. Wiaderek, K. W. Chapman, C. J. Pickard, A. J. Morris, and C. P. Grey, "Investigating sodium storage mechanisms in tin anodes: A combined pair distribution function analysis, density functional theory, and solid-state NMR approach," *J. Am. Chem. Soc.*, vol. 139, no. 21, pp. 7273–7286, 2017.

[55] Y. Wang, J. Lv, L. Zhu, and Y. Ma, "Crystal structure prediction via particle-swarm optimization," *Phys. Rev. B*, vol. 82, p. 094116, 2010.

[56] D. M. Deaven and K. M. Ho, "Molecular geometry optimization with a genetic algorithm," *Phys. Rev. Lett.*, vol. 75, pp. 288–291, 1995.

[57] G. Hautier, C. C. Fischer, A. Jain, T. Mueller, and G. Ceder, "Finding nature's missing ternary oxide compounds using machine learning and density functional theory," *Chem. Mater.*, vol. 22, no. 12, pp. 3762–3767, 2010.

[58] M. K. Aydinol, A. F. Kohan, G. Ceder, K. Cho, and J. Joannopoulos, "Ab initio study of lithium intercalation in metal oxides and metal dichalcogenides," *Phys. Rev. B*, vol. 56, pp. 1354–1365, 1997.

[59] L. E. Marbella, M. L. Evans, M. F. Groh, J. Nelson, K. J. Griffith, A. J. Morris, and C. P. Grey, "Sodiation and desodiation via helical phosphorus intermediates in high-capacity anodes for sodium-ion batteries," *J. Am. Chem. Soc.*, vol. 140, no. 25, pp. 7994–8004, 2018.

[60] M. M. Butala, M. Mayo, V. V. T. Doan-Nguyen, M. A. Lumley, C. Göbel, K. M. Wiaderek, O. J. Borkiewicz, K. W. Chapman, P. J. Chupas, M. Balasubramanian, G. Laurita, S. Britto, A. J. Morris, C. P. Grey, and R. Seshadri, "Local structure evolution and modes of charge storage in secondary Li–FeS_2 cells," *Chem. Mater.*, vol. 29, no. 7, pp. 3070–3082, 2017.

[61] S. P. Gordienko and G. Sh Viksman, "Methods of investigation and properties of powder materials high-temperature behavior and thermodynamic properties of the compounds Cu_3P and CuP_2,"

[62] O. Oloffson, "The Crystal Structure of Cu_3P," *Acta Chemica Scandanavia*, vol. 26, no. 7, pp. 2777–87, 1972.

[63] M. M. H. and J. W., "Darstellung, eigenschaften und kristallstruktur von Cu_2P_7 und strukturverfeinerungen von CuP_2 und AgP_2," *Zeitschrift für anorganische und allgemeine Chemie*, vol. 491, no. 1, pp. 225–236, 1982.

[64] M. E. Schlesinger, "The thermodynamic properties of phosphorus and solid binary phosphides," *Chem. Rev.*, vol. 102, no. 11, pp. 4267–4302, 2002.

[65] L.-M. Yang and E. Ganz, "Adding a new dimension to the chemistry of phosphorus and arsenic," *Physical Chemistry Chemical Physics*, vol. 18, no. 26, pp. 17586–17591, 2016.

[66] B. Mauvernay, M.-L. Doublet, and L. Monconduit, "Redox mechanism in the binary transition metal phosphide Cu_3P," *J. Phys. Chem. Sol.*, vol. 67, no. 5-6, pp. 1252–1257, 2006.

[67] G. A. Li, C. Y. Wang, W. C. Chang, and H. Y. Tuan, "Phosphorus-Rich Copper Phosphide Nanowires for Field-Effect Transistors and Lithium-Ion Batteries," *ACS Nano*, vol. 10, no. 9, pp. 8632–8644, 2016.

[68] L. De Trizio, R. Gaspari, G. Bertoni, I. Kriegel, L. Moretti, F. Scotognella, L. Maserati, Y. Zhang, G. C. Messina, M. Prato, S. Marras, A. Cavalli, and L. Manna, "$Cu_{3-x}P$ nanocrystals as a material platform for near-infrared plasmonics and cation exchange reactions," *Chem. Mater.*, vol. 27, no. 3, pp. 1120–1128, 2015.

[69] C. J. Pickard, "On-the-fly pseudopotential generation in CASTEP," *University of St. Andrews*, (Document Online) September 2006.

[70] A. van de Walle, Z. Moser, and W. Gasior, "First-principles calculation of the Cu-Li phase diagram," *Archives of Metallurgy and Materials*, vol. 3, no. 49, pp. 535,544, 2004.

[71] H. Okamoto, "Supplemental Literature Review of Binary Phase Diagrams: Ag-Li, Ag-Sn, Be-Pu, C-Mn, C-Si, Ca-Li, Cd-Pu, Cr-Ti, Cr-V, Cu-Li, La-Sc, and Li-Sc," *Journal of Phase Equilibria and Diffusion*, vol. 38, no. 1, pp. 70–81, 2017.

[72] M. Mendelsohn, A. Krauss, and D. Gruen, "Preparation and some properties of cu-li alloys containing up to 20 at.% Li," tech. rep., Argonne National Lab., 1985.

[73] C. F. Old and P. Trevena, "Reaction in copper-lithium system and its implications for liquid-metal embrittlement," *Metal Science*, vol. 15, no. 7, pp. 281–286, 1981.

[74] A. Penaloza, M. Ortiz, and C. Worner, "An electrodeposition method to obtain Cu-Li alloys," *J. Mater. Sci. Lett.*, vol. 14, pp. 511–513, 1995.

[75] W. Gąsior, B. Onderka, Z. Moser, A. Dębski, and T. Gancarz, "Thermodynamic evaluation of Cu–Li phase diagram from EMF measurements and DTA study," *Calphad*, vol. 33, no. 1, pp. 215 – 220, 2009.

[76] S. Grugeon, S. Laruelle, R. Herrera-Urbina, L. Dupont, P. Poizot, and J. Tarascon, "Particle size effects on the electrochemical performance of copper oxides toward lithium," *Journal of The Electrochemical Society*, vol. 148, no. 4, pp. A285–A292, 2001.

[77] C. M. Sweeney, K. L. Stamm, and S. L. Brock, "On the feasibility of phosphide generation from phosphate reduction: The case of Rh, Ir, and Ag," *J. Alloy. Comp.*, vol. 448, no. 1, pp. 122 – 127, 2008.

[78] H. Jung, P. K. Allan, Y.-Y. Hu, O. J. Borkiewicz, X.-L. Wang, W.-Q. Han, L.-S. Du, C. J. Pickard, P. J. Chupas, K. W. Chapman, A. J. Morris, and C. P. Grey, "Elucidation of the local and long-range structural changes that occur in germanium anodes in lithium-ion batteries," *Chem. Mater.*, vol. 27, no. 3, pp. 1031–1041, 2015.

[79] A. Schiele, T. Hatsukade, B. B. Berkes, P. Hartmann, T. Brezesinski, and J. Janek, "High-throughput in situ pressure analysis of lithium-ion batteries," *Analytical Chemistry*, vol. 89, no. 15, pp. 8122–8128, 2017.

[80] Y. M. Goryachev, V. B. Chernogorenko, and L. I. Fiyalka, "Electron parameters and thermodynamics of phases in the copper-oxygen-phosphorus system," *Powder Metallurgy and Metal Ceramics*, vol. 37, pp. 1–2, 1998.

[81] L. Wang, Z. Jiang, W. Li, X. Gu, and L. Huang, "Hybrid phosphorene/graphene nanocomposite as an anode material for Na-ion batteries: a first-principles study," *J. Phys. D: Appl. Phys.*, vol. 50, no. 16, p. 165501, 2017.

[82] S. Boyanov, J. Bernardi, F. Gillot, L. Dupont, M. Womes, J.-M. Tarascon, L. Monconduit, and M.-L. Doublet, "FeP: another attractive anode for the Li-ion battery enlisting a reversible two-step insertion/conversion process," *Chemistry of materials*, vol. 18, no. 15, pp. 3531–3538, 2006.

[83] R. Soulairol, C.-C. Fu, and C. Barreteau, "Structure and magnetism of bulk Fe and Cr: from plane waves to LCAO methods," *J. Phys. Cond. Mat.*, vol. 22, no. 29, p. 295502, 2010.

[84] J.-H. Cho and M. Scheffler, "Ab initio pseudopotential study of Fe, Co, and Ni employing the spin-polarized LAPW approach," *Phys. Rev. B*, vol. 53, pp. 10685–10689, 1996.

[85] E. G. Moroni, G. Kresse, J. Hafner, and J. Furthmüller, "Ultrasoft pseudopotentials applied to magnetic Fe, Co, and Ni: From atoms to solids," *Phys. Rev. B*, vol. 56, pp. 15629–15646, 1997.